Neuron

Article

Voltage imaging reveals circuit computations in the raphe underlying serotonin-mediated motor vigor learning

Highlights

- Serotonergic dorsal raphe neurons encode action effectiveness in motor vigor learning
- Motor learning requires coincidence detection of actions and their outcomes
- Voltage and transmitter imaging show coincidence detection via post-inhibitory rebound
- Action effectiveness encoding and motor learning depend on GABAergic inhibition

Authors

Takashi Kawashima, Ziqiang Wei, Ravid Haruvi, Inbal Shainer, Sujatha Narayan, Herwig Baier, Misha B. Ahrens

Correspondence

takashi.kawashima@weizmann.ac.il (T. K.),
weiz@janelia.hhmi.org (Z.W.),
ahrensm@janelia.hhmi.org (M.B.A.)

In brief

Kawashima et al. show, through voltage and neurotransmitter imaging in larval zebrafish, that serotonergic neurons in the dorsal raphe nucleus compute action effectiveness during motor learning by associating actions with their outcomes. Each action induces inhibition, then rebound, during which visual outcomes trigger neural spikes conveying action effectiveness, enabling motor learning.

Kawashima et al., 2025, Neuron *113*, 1–16
August 20, 2025
https://doi.org/10.1016/j.neuron.2025.05.017

CellPress

Please cite this article in press as: Kawashima et al., Voltage imaging reveals circuit computations in the raphe underlying serotonin-mediated motor vigor learning, Neuron (2025), https://doi.org/10.1016/j.neuron.2025.05.017

Neuron

CellPress
OPEN ACCESS

Article

Voltage imaging reveals circuit computations in the raphe underlying serotonin-mediated motor vigor learning

Takashi Kawashima,[1,2,4,*] Ziqiang Wei,[1,4,*] Ravid Haruvi,[2] Inbal Shainer,[2,3] Sujatha Narayan,[1] Herwig Baier,[3] and Misha B. Ahrens[1,5,*]
[1]Janelia Research Campus, Howard Hughes Medical Institute, Ashburn, VA 20147, USA
[2]Department of Brain Sciences, Weizmann Institute of Science, Rehovot 7610001, Israel
[3]Max Planck Institute for Biological Intelligence, Martinsried 82152, Germany
[4]These authors contributed equally
[5]Lead contact
*Correspondence: takashi.kawashima@weizmann.ac.il (T.K.), weiz@janelia.hhmi.org (Z.W.), ahrensm@janelia.hhmi.org (M.B.A.)
https://doi.org/10.1016/j.neuron.2025.05.017

SUMMARY

As animals adapt to new situations, neuromodulation is a potent way to alter behavior, yet mechanisms by which neuromodulatory nuclei compute during behavior are underexplored. The serotonergic raphe supports motor learning in larval zebrafish by visually detecting distance traveled during swims, encoding action effectiveness, and modulating motor vigor. We tracked the raphe's input-output computations at millisecond timescales using voltage and neurotransmitter imaging and found that swimming opens a gate for visual input to cause spiking in serotonergic neurons, enabling the encoding of action outcomes and filtering out learning-irrelevant visual signals. Specifically, swim commands initially inhibited serotonergic neurons via γ-aminobutyric acid (GABA). Immediately after, membrane voltage increased via post-inhibitory rebound, allowing swim-induced visual motion to evoke firing through glutamate, triggering serotonin release to modulate future motor vigor. Ablating local GABAergic neurons impaired raphe coding and motor learning. Thus, serotonergic neuromodulation arises from action-outcome coincidence detection within the raphe.

INTRODUCTION

Neuromodulation alters behavior, allowing animals to adapt to changes in their environment and adjust to unexpected signals from body organs.[1] These behavioral adjustments occur as secreted neuromodulators bind to receptors on neurons and astrocytes, shaping circuit dynamics.[2,3] While much research has focused on understanding the effects of neuromodulation on circuit dynamics and behavior, as well as the computational interpretation of variables encoded in the spike patterns of neuromodulatory cells,[4] there remains a gap in our knowledge of how internal circuits within neuromodulatory nuclei process information during behavior. To trigger behavioral adjustments, how do cells within these nuclei interact with one another to transform input signals into precisely timed neurotransmitter release?

A significant behavioral change occurs when animals adjust their motor commands to meet the demands of dynamic environments. For example, larval zebrafish learn and adapt motor vigor to changes in the effectiveness by which motion of their tail propels their body forward (i.e., action effectiveness) by monitoring the distance traveled per swim.[5,6] While passive displacement of the fish's location can impact subsequent swimming,[7] only self-produced displacements should drive motor learning, while non-self-produced displacements should not impact motor learning. More generally, learning action effectiveness requires animals to use temporal correlations between actions and feedback to accurately determine action outcomes to be used in motor learning. Neural mechanisms of motor learning are distributed across the brain,[8–10] including neuromodulatory systems.[11–13] The vertebrate serotonergic system modulates motor learning at various levels, from enhancing sensory perception to directly suppressing spinal cord outputs.[14] Such modulation can have differential effects depending on behavioral context.[15,16]

In zebrafish, serotonergic neurons in the dorsal raphe nucleus (DRN) contribute to motor vigor learning. Serotonergic neurons continuously track the sensory outcomes of swimming, such as the distance traveled per swim bout, update an internal estimate of action effectiveness in memory represented by their spike rates, and modulate future motor vigor.[17] Yet, it remains unknown how these motor-sensory computations—including motor-gated sensory coding that isolates action outcomes from other stimuli—occur via network and cellular interactions, specifically within the serotonergic system. Such insights are necessary to understand how the vertebrate serotonergic system integrates multiple streams of sensory and motor information to control behavior.[4,18–23]

Please cite this article in press as: Kawashima et al., Voltage imaging reveals circuit computations in the raphe underlying serotonin-mediated motor vigor learning, Neuron (2025), https://doi.org/10.1016/j.neuron.2025.05.017

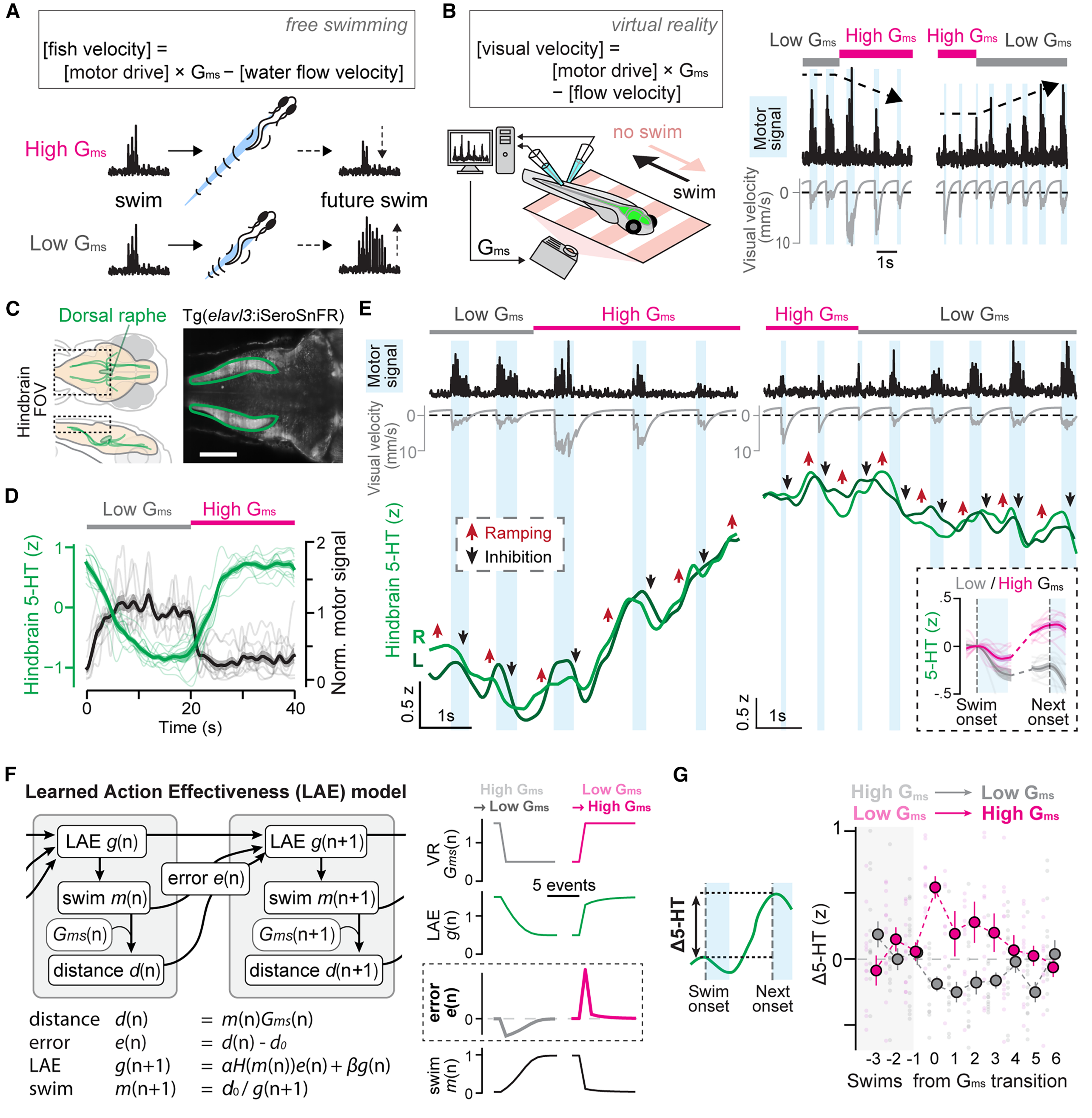

Figure 1. 5-HT release pattern during motor vigor learning reflects learning of action effectiveness

(A) Schematic of motor adaptation in response to changes in action effectiveness (G_{ms}). To uphold a constant traveled distance per action, animals adapt by intensifying their effort per action in low G_{ms} and reducing it in high G_{ms}.

(B) Left: experimental setup with VR environment with visual feedback determined via G_{ms}. Right: larval zebrafish adapt their swim vigor in the VR environment in response to changes in the amount of visual feedback upon transitions between low and high G_{ms}.

(C) Schematic of the zebrafish raphe serotonergic system (left) and an image of pan-neuronal 5-HT indicator expression in *Tg(elavl3:iSeroSnFR)* in regions of interest in the hindbrain neuropil (right). Scale bar, 100 μm.

(D) Swim vigor adaptation (black) and *Z* scored 5-HT release in the hindbrain (green) during transitions between low and high G_{ms}. Shading represents standard error of the mean (SEM) across *N* = 9 fish.

(E) Zoomed-in 5-HT signals during individual swim events, taken from the behavioral transitions shown in (B), exhibit an initial inhibition during swimming (black arrows), followed by an increase immediately after (red arrows). L and R indicate 5-HT release on the left and right sides of the hindbrain, respectively. Inset: 5-HT release patterns averaged around swim events, showing post-swim increase at high G_{ms} and decrease at low G_{ms}. Shading represents SEM across *N* = 9 fish.

(legend continued on next page)

Here, we investigated the input-output transformations and the underlying millisecond-timescale mechanisms of DRN serotonergic neurons during motor vigor learning in larval zebrafish by using a suite of genetically encoded voltage and neurotransmitter indicators. Specifically, we asked how the DRN computes the outcomes of actions and uses them to create a representation of action effectiveness—by responding only to visual feedback resulting from motor actions (relevant for motor learning) while filtering out visual input unrelated to motor actions (irrelevant for learning). Generalized forms of this mechanism of action-outcome computation may operate in the vertebrate serotonergic system across behavioral contexts.

RESULTS

Zebrafish serotonergic system learns action effectiveness to adapt motor vigor

To measure how the serotonergic system computes action effectiveness for each swim event in zebrafish, we built on previous work showing that serotonergic neurons in the raphe nucleus integrate action effectiveness over time and modulate motor vigor.[17] We measured axonal serotonin (5-HT) release from the DRN while the fish performed a motor vigor learning task (Figure 1A) in a virtual reality (VR) environment. In this virtual visual environment (Figure 1B), a paralyzed head-fixed fish swam against a virtual water current, with the current simulated by forward motion of the visual environment projected on a screen beneath the fish. Their swim signals were detected from the spinal cord through a pair of electrodes attached to the tail. When a swim signal was detected, forward movement of the fish was simulated by transient backward motion of the visual environment. The velocity and distance moved as a result of swimming were proportional to the amplitude of detected swim signals, scaled by motosensory gain (G_{ms}), which represents action effectiveness. Motosensory gain can be manipulated to induce motor vigor learning.[5,6] Fish adapted the amplitudes of swimming signals in response to changes in G_{ms} in a compensatory manner: low G_{ms} induced progressively stronger swimming, and high G_{ms} induced progressively weaker swimming (Figure 1B, right).

We examined the 5-HT dynamics during this motor learning task by imaging 5-HT release in the hindbrain from DRN serotonergic neurons using a genetically encoded indicator, iSeroSnFR (Figure 1C), and a light-sheet microscope. This indicator[24,25] has fast kinematics (τ_{decay} = 150 ms) and is suited for capturing subsecond dynamics of 5-HT release. In a motor adaptation task where G_{ms} transitioned between low and high values every 20 s, fish adapted and equilibrated their swim vigor over a period of ∼10 s after the transition (Figure 1D). Consistent with calcium imaging in DRN serotonergic neurons,[17] 5-HT levels were lower as fish swam with stronger swim vigor in low G_{ms} than when they swam with weaker swim vigor in high G_{ms} (Figure 1D). At a finer timescale, 5-HT levels showed a transient decrease during every swim bout, then gradually rose between swims (Figure 1E). After each swim, the rise in 5-HT was greater during high G_{ms}, leading to a gradual overall increase. By contrast, at low G_{ms}, the post-swim rise was smaller, leading to an overall decrease in 5-HT levels (Figures 1E and S1A), suggesting that 5-HT levels tracked an internal estimate of action effectiveness. This change in 5-HT levels after swimming is predictive of the vigor of the next swim bout (Figure S1B), suggesting that the internal estimate of action effectiveness drives motor adaptation in zebrafish.

To normatively explain this form of motor learning, we developed the learned action effectiveness (LAE) model (Figure 1F) and compared its predictions with the temporal dynamics of 5-HT release. In this model, the actual travel distance after an n^{th} swim bout, $d(n)$, estimated from the visual flow during and right after a swimming event $m(n)$, is compared against a desired travel distance (constant d_0). The error $e(n) = d(n) - d_0$ is used to update the learned estimate of action effectiveness $g(n+1)$. Fish generate the next swim event with vigor $m(n+1)$ based on the desired travel distance d_0 and estimated action effectiveness $g(n+1)$. This $g(n+1)$ is only updated when there is a motor action, captured by the Heaviside function, H, which equals 1 when its argument is positive and 0 otherwise, and decays over time with a retention coefficient β. We included H and β in the model to explain our previous observations of sensory gating—in which DRN serotonergic neurons only respond to visual motion if it occurs within a short time window following a motor command—and the slow decay of tonic firing during the short-term motor learning task.[17] We simulated the model during transitions between high and low G_{ms} (Figure 1F, right) and compared the temporal dynamics of LAE $g(n)$ and error signal $e(n)$ to the temporal dynamics of 5-HT release. The dynamics of $g(n)$ in the model and the 5-HT release showed similar patterns at slower timescales (Figures 1D and 1F). Notably, the error signal $e(n)$ qualitatively mimicked the change of 5-HT levels between swim bouts (Δ5-HT) after changes in G_{ms} (Figures 1F and 1G). Such similarity could not be obtained by models that do not include error computation (Figure S1C). These results suggest that temporal dynamics of 5-HT release encode an internal estimate of LAE during motor learning.

We also investigated whether the LAE model predicts the experimental observation that the loss of serotonergic neurons impairs short-term motor learning effects observed in our previous study (Figure S1D)[17] by simulating the LAE model with a low retention coefficient β (Figure S1E). With this parameter setting, the model predicts less suppression of motor vigor during high-G_{ms} training, and a loss of effect of training duration on swimming after a delay period, i.e., reduced memory (Figure S1E). This prediction qualitatively matched the behavioral effects of chemogenetically ablating DRN *tph2+* serotonergic neurons (Figure S1F). Thus, the LAE model successfully predicted the fast dynamics of 5-HT release during motor vigor learning

(F) Schematic (top) and algorithmic implementation (bottom) of the learned action effectiveness (LAE) model. Parameters: α, learning rate; β, retention factor; d_0, desired distance (a constant) to travel per swim. Our model updates at every swim event n. Right: simulations of an LAE model during 10 swim events at transitions between low G_{ms} and high G_{ms}.

(G) Swim-by-swim increase of 5-HT release (Δ5-HT; *Z* scored) at the transitions of G_{ms} in our experiments qualitatively matches the error term *e*(n) in the LAE model. Error bars represent SEM across *N* = 9 fish. See also Figure S1.

Please cite this article in press as: Kawashima et al., Voltage imaging reveals circuit computations in the raphe underlying serotonin-mediated motor vigor learning, Neuron (2025), https://doi.org/10.1016/j.neuron.2025.05.017

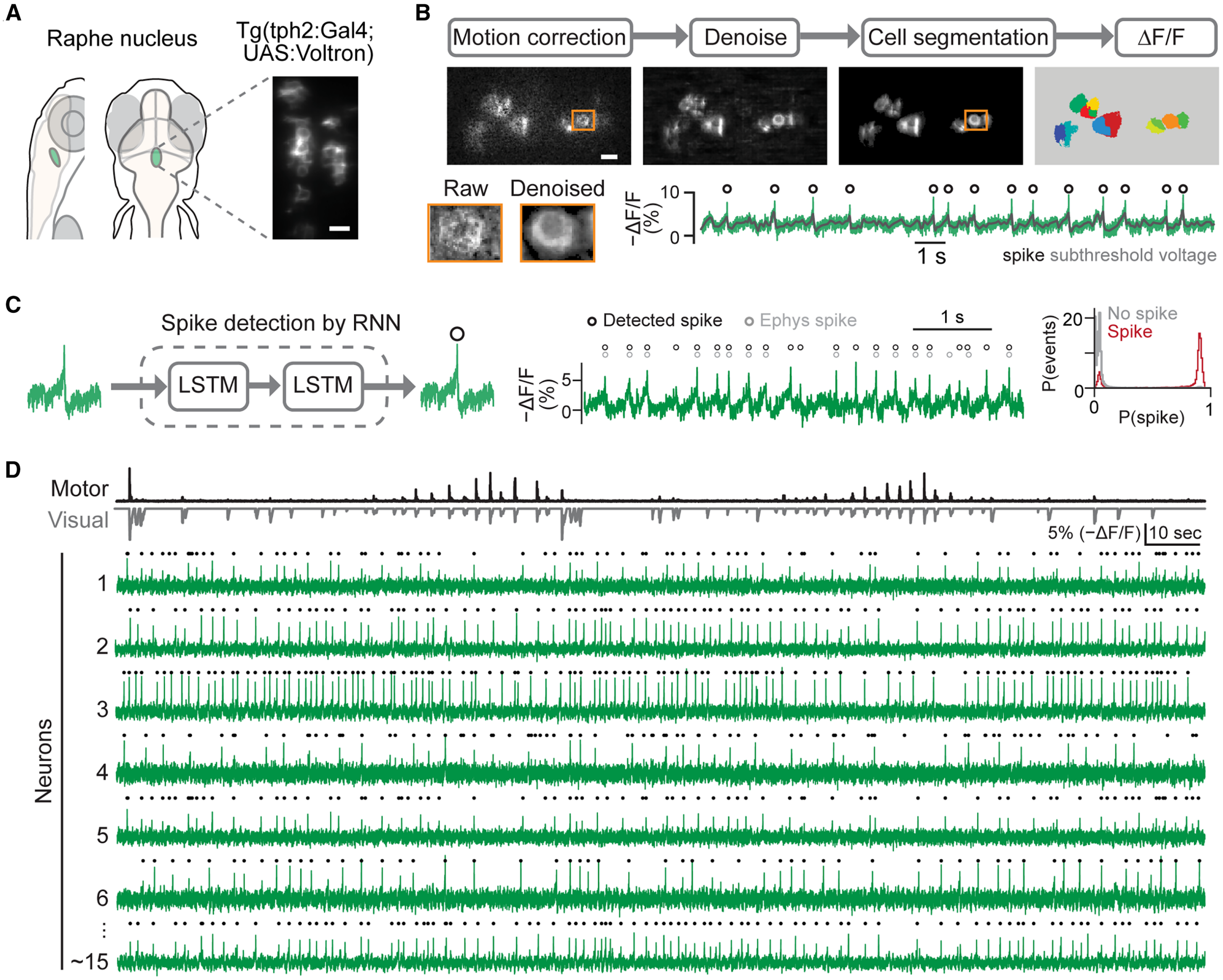

Figure 2. Voltage imaging in the serotonergic raphe during motor vigor learning

(A) The anatomical location of the serotonergic raphe and the expression of the Voltron indicator in *tph2*+ neurons visualized by JF525 dye staining. Scale bar, 10 μm.

(B) Top: schematic of pre-processing pipeline: motion correction, denoising, cell segmentation, and ΔF/F calculation. Scale bar, 10 μm. Bottom: the effects of denoising for a representative neuron from the top panel on the image pixel weights (left) and estimated voltage signals (right).

(C) Spike-detection artificial neural network and validation with electrophysiology. Left: schematic of the neural network. Center: spikes detected by voltage imaging (black) and simultaneous loose-patch electrophysiology (gray) (Figure S2A). Right: spike-detection performance. The probability of a detected spike, P(spike), is shown for the case of no-spike events (gray) and spike events (red) categorized by the electrophysiology data.

(D) Voltage imaging of serotonergic neurons during motor vigor learning. Top: motor signals (black) and visual feedback during swimming (gray). Bottom: representative traces of voltage in simultaneously recorded serotonergic neurons with detected spikes. See also Video S1.

(Figures 1F and 1G) as well as the behavioral phenotypes of the ablation of raphe serotonergic neurons in the short-term motor learning task (Figures S1E and S1F).[17] These results suggest that the raphe serotonergic neurons in zebrafish encode LAE to modulate future actions and motivated us to unravel the circuit and cellular mechanisms of the neural computations.

Voltage imaging of membrane potential and spiking activity reveals single-cell and population dynamics of DRN serotonergic neurons

To understand neural computations underlying the fast 5-HT dynamics, we used a chemigenetic voltage indicator, Voltron,[26] to record membrane voltage signals from populations of raphe serotonergic neurons during motor vigor learning (Figure 2). Unlike calcium imaging, which has limited temporal resolution and cannot directly report inhibition,[27] voltage imaging allows us to track changes in membrane potential and spiking activity at the millisecond timescale. We used a transgenic zebrafish that expresses Voltron sparsely in *tph2*+ neurons in the DRN and performed voltage imaging at a speed of 300 Hz (Figure 2A). We created a custom pipeline to automate the imaging processing with motion correction, denoising, cell segmentation, and ΔF/F extraction to collect membrane potential and spiking dynamics from individual neurons (Figure 2B; Video S1). We created a

Please cite this article in press as: Kawashima et al., Voltage imaging reveals circuit computations in the raphe underlying serotonin-mediated motor vigor learning, Neuron (2025), https://doi.org/10.1016/j.neuron.2025.05.017

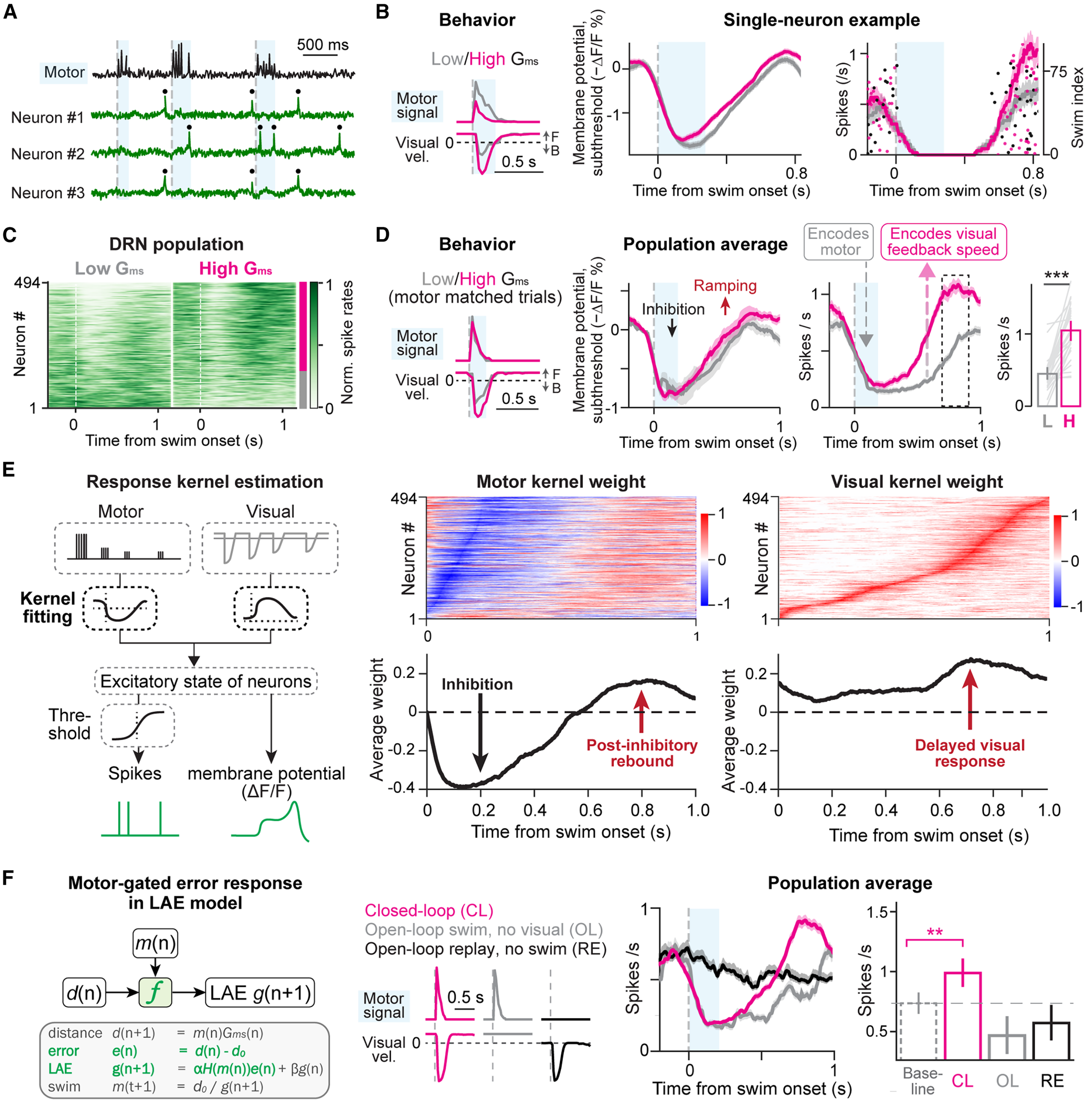

Figure 3. Membrane potential and spiking activity of serotonergic neurons show gain encoding and motor-gated sensory responses

(A) Swim signals and voltage signals from three simultaneously recorded neurons during motor vigor learning.

(B) Neural activity at different G_{ms} from an example serotonergic neuron. Left: average swim signals and visual motion at the onset of swim events for different G_{ms} conditions; center: membrane potential; and right: spike events (dots) and spike rates (lines). "F" stands for forward visual motion, "B" for backward motion. Shading represents SEM across swim events.

(C) Average spike rates of all recorded serotonergic neurons at the onset of swimming for low- and high-G_{ms} conditions. 349 high-G_{ms} cells (magenta) and 145 low-G_{ms} cells (gray) from 21 fish.

(D) The velocity of visual feedback is encoded in the post-swim firing rate. Left: average behavioral traces. We sub-selected trials to equalize motor vigor under different G_{ms} conditions. Center: average subthreshold and spiking responses. The dashed box represents the time window for quantifying spike rates. Right: spike rates after swimming under different G_{ms}. $^{***}p < 1.0 \times 10^{-4}$ for the effect of G_{ms} by two-way ANOVA. $N = 4$ fish, 29 high-G_{ms} cells. Shading represents SEM across cells.

(E) Fitting of a spiking kernel model (left) revealed that swimming triggers an initial inhibition and a post-inhibitory rebound, whereas visual feedback triggers a delayed excitation after swimming.

(legend continued on next page)

Please cite this article in press as: Kawashima et al., Voltage imaging reveals circuit computations in the raphe underlying serotonin-mediated motor vigor learning, Neuron (2025), https://doi.org/10.1016/j.neuron.2025.05.017

deep neural network for detecting spiking signals, which was trained using datasets of simultaneous voltage imaging and juxtacellular electrophysiology in zebrafish.[26] The trained network recognized electrically recorded spikes with high accuracy (Figures 2C and S2A). With these analysis pipelines, we were able to extract membrane potential dynamics and spiking activity simultaneously from ∼15 DRN neurons (Figure 2D) to investigate how these neurons combine motor and sensory signals and enable motor vigor learning.

Motor-gated sensory coding during motor vigor learning

To investigate how DRN serotonergic neurons respond selectively to sensory feedback from swims—while filtering out stimuli that do not coincide with swimming—we examined how the activity of DRN serotonergic neurons is modulated by individual swim events (Figure 3A) by analyzing swim-evoked averages of membrane potential and spiking activity. We observed, in individual neurons, a suppression of membrane potential and spike rates during swims, followed by an increase in voltage and spiking after swims (Figures 3B and S2B), in concordance with 5-HT dynamics (Figure 1E). The post-swim increase in spiking was higher during high G_{ms}, consistent with the encoding of the action effectiveness in the LAE model (Figures 1F and 1G). This spiking pattern held true across most of the population of DRN neurons, apart from a smaller fraction of neurons that had higher firing rates during low G_{ms} (Figure 3C). To disentangle the contribution of motor and sensory inputs to the post-swim response, we selected swim bouts of similar vigor in both G_{ms} conditions, and found that the post-swim firing rate reflected G_{ms} and the speed of visual feedback (Figure 3D). The increase in firing rate was fractionally larger than the increase in membrane potential due to the averaging of post-spike hyperpolarization seen in most DRN neurons (Figure 2C). Thus, during-swim hyperpolarization results from swim events, and post-swim spiking encodes the speed of visual feedback.

We also estimated the temporal response kernel of DRN neurons to motor and visual inputs by fitting a model of membrane potential modulation and spiking activity to all recorded neurons (Figure 3E). The estimated motor response kernel reflected inhibition in the early phase relative to swim times, and the estimated visual response kernel reflected late-phase responses to visual motion feedback (Figures 3E and S2C). Additionally, a post-swim "rebound" appeared in the motor response kernel (Figure 3E), suggestive of a biophysical mechanism by which swimming first induces inhibition, followed by a post-inhibitory rebound in serotonergic neurons. It also suggests that, during the rebound period, visual excitation causes the cells to fire proportionally to visual speed. This suggests a mechanism by which the rebound by itself raises membrane potential but not enough to cause spiking. Similarly, visually evoked excitation is insufficient to trigger spiking, but when they coincide, they together elevate the voltage above the firing threshold, allowing serotonergic neurons to encode visual speed in a small time window following motor commands. Evidence of rebound in DRN neurons has been observed,[28] which may occur through a variety of mechanisms.[29–33] Thus, a predictive model fit disentangles motor and visual contributions to the firing patterns of serotonergic neurons and suggests a mechanistic substrate for the way they transform motor-sensory inputs into spikes and 5-HT release.

We asked whether this temporal coincidence of the swim-evoked rebound and visually evoked excitation is necessary for evoking spiking activity (Figure 3F). Our previous work using calcium imaging indicated that DRN serotonergic neurons respond only to visual input when it occurs in a precise window right after swim commands,[17] which, together with delays in visual input due to processing in visual centers, corresponds to the period when the fish receives visual motion feedback during late-phase swimming and the following coasting period. As before, this coincidence detection is represented as a Heaviside function of action in the LAE model, which is 1 as fish swim and 0 otherwise (Figures 1F and 3F). Thus we investigated the membrane potential and spiking activity of serotonergic neurons under three conditions: (1) swimming with visual feedback, (2) swimming without visual feedback, and (3) replayed visual feedback without swimming. Whereas swimming with feedback increased post-swim spikes, visual input without swimming elicited no change in spiking (Figures 3F and S2D). Swimming without feedback caused the dip in firing rate during swimming but did not elicit post-swim spiking (Figure 3F). Strong swim vigor resulted in stronger post-inhibitory rebound in the membrane potential (Figure S2E). These data support the necessity of the temporal coincidence between swimming-induced post-inhibitory rebound and visually induced excitation for the encoding of action effectiveness in the spiking activity of serotonergic neurons. Thus, through a mechanism of temporal coincidence detection, DRN serotonergic neurons effectively filter out sensory inputs that are irrelevant to motor vigor learning and encode learning-relevant signals in post-swim spiking.

To examine serotonergic neural activity over longer timescales, we performed voltage imaging during a short-term motor learning task[17] in which fish reduced their swim vigor under high G_{ms} and maintained it during a delay. Voltage imaging, along with the LAE model and calcium imaging,[17] indicated that LAE is represented in persistent spiking activity of serotonergic neurons following prolonged exposure to high G_{ms} (Figure S2F). Consistent with DRN activity and the LAE model, fish successfully learned high G_{ms} only when visual motion was coupled to their swimming, and learning failed when visual motion was not self-generated, even if identical visual motion sequences were passively replayed from earlier trials (Figure S3). Thus, DRN serotonergic neurons filter out sensory inputs that are not directly related to the animal's own actions to correctly encode and store

(F) Spiking response of serotonergic neurons to visual feedback is gated by motor actions. Left: gating as part of the LAE model presented in Figure 1F. Center: behavioral traces during three trial types: closed-loop swimming with visual feedback (magenta), swimming only without visual feedback (gray), and visual input only (black, a replay of the visual motion from a previous closed-loop trial). Trials are sub-selected to equalize the swim vigors between the first two conditions. Shading represents SEM across cells. 51 high-G_{ms} cells from $N = 7$ fish. Right: spike rates show significant differences across trial types, $p = 5.4 \times 10^{-7}$ two-way ANOVA, and no significant difference across fish identity. $^{**}p = 0.00018$ by the paired signed-rank test of pre-swim vs. post-swim spike rates with Bonferroni correction. Error bars represent SEM across the same set of cells. See also Figure S2.

Please cite this article in press as: Kawashima et al., Voltage imaging reveals circuit computations in the raphe underlying serotonin-mediated motor vigor learning, Neuron (2025), https://doi.org/10.1016/j.neuron.2025.05.017

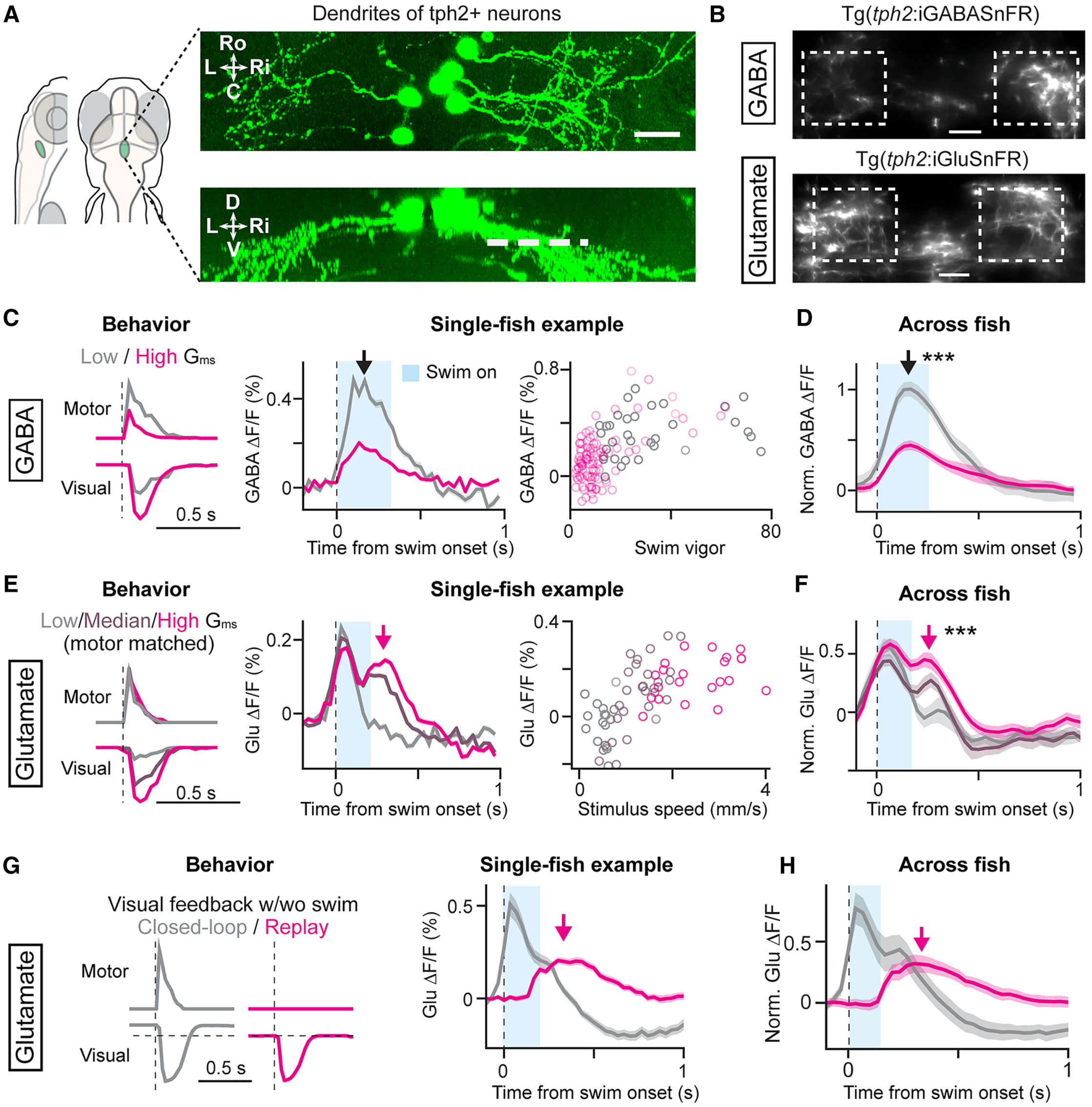

Figure 4. The sources of inhibitory and excitatory inputs on the dendrites of serotonergic neurons

(A) Morphology of raphe serotonergic neurons and their dendrites in zebrafish. The approximate location of the dendritic imaging plane is indicated by a dashed line. Ro, rostral; C, caudal; L, left; Ri, right; D, dorsal; V, ventral. Scale bar, 20 μm.

(B) Images of GABA indicator and glutamate indicator expressed in the dendrites of serotonergic neurons. Scale bar, 20 μm.

(C and D) Dendritic GABA inputs during motor vigor learning. GABA signals encode the swim vigor of individual swim bouts, with stronger GABA signals observed during strong bouts in low G_{ms}. (C) example from a single fish. (D) Summary of 12 sessions from 4 fish. Three different axial planes were imaged per fish. Shading represents SEM across trials in (C) and across sessions in (D). $^{***}p < 0.001$, paired signed-rank test for the peak amplitudes.

(E and F) Dendritic glutamate inputs during swim bouts with various visual feedback speeds randomly given at low, medium, or high G_{ms}. Swim events were sub-selected to equalize motor vigor among different G_{ms} conditions. (E) Example from a single fish. (F) Summary of 25 sessions from 9 fish. Two or three different axial planes were imaged per fish. Shading represents SEM across trials in (E) and across sessions in (F). $^{***}p < 0.001$, paired signed-rank test across all 3 paired G_{ms} groups for the second peak.

(G) Visually evoked glutamate inputs occur in the absence of motor actions. Example from a single fish. We sub-selected swim events so that the speed of visual feedback equalizes across conditions. Gray, closed-loop trial; magenta, replay trial with no swimming. Note that during the replay, forward visual flow was replaced by zero visual flow to prevent swimming, which is the likely cause for the difference in the late-phase glutamate signal. Shading represents SEM across trials.

(H) Across-fish average of glutamate inputs in response to closed-loop feedback during swimming (gray) or replay of visual feedback (magenta) shown in (G). $N = 6$ fish, 17 sessions. Shading represents SEM across sessions. See also Figure S4.

Please cite this article in press as: Kawashima et al., Voltage imaging reveals circuit computations in the raphe underlying serotonin-mediated motor vigor learning, Neuron (2025), https://doi.org/10.1016/j.neuron.2025.05.017

only those action-outcome relationships that are relevant for motor learning.

The sources of inhibitory and excitatory inputs on the dendrites of serotonergic neurons

We sought to identify the pathways of motor and visually driven inputs[34] that determine responses of raphe serotonergic neurons by using genetically encoded neurotransmitter indicators (Figure 4). Serotonergic raphe neurons receive both GABAergic and glutamatergic inputs.[35] Thus we expressed a GABA indicator (iGABASnFR)[36] or a glutamate indicator (iGluSnFR)[37] in *tph2*+ serotonergic neurons (Figures 4A and 4B) and imaged their dendrites to monitor excitatory and inhibitory inputs during motor vigor learning. We observed a "wave" of GABAergic input during swimming, whose amplitude increased when swim vigor increased at low G_{ms}. This indicates that GABAergic inputs to serotonergic neurons during swimming encode motor vigor (Figures 4C and 4D). These GABAergic inputs likely originate from local GABAergic neurons in the DRN, which encode the vigor of swimming (Figures S4A and S4B)[17] and may monosynaptically inhibit serotonergic neurons.[38] The timing of the GABA signal (Figure 4C) was coincident with the timing of the decrease in the membrane voltage of serotonergic neurons (Figure 3D). Conversely, glutamate input was present in two waves, the first wave occurring around the time of swimming and the second one occurring immediately after swimming (Figures 4E, 4F, S4C, and S4D). The first wave reflected the motor command, or efference copy, and started slightly before swimming, and the second wave peaked after the swims. The fact that the first glutamate wave did not cause a concurrent rise in the membrane potential of serotonergic neurons (Figure 3) suggests that it could be a spillover from nearby axons that do not target synapses on the dendrites of serotonergic neurons or that the glutamatergic excitation is masked by GABAergic inhibition in the early phase.

The onset of the second glutamate wave coincided with the onset of the voltage ramp in serotonergic neurons (Figure 3D), consistent with glutamate being the driver of the late-phase voltage increase. This second wave reflected the speed of visual feedback, proportional to G_{ms} (Figures 4E and 4F), consistent with the 5-HT neurons' spiking responses and 5-HT release (Figures 1E and 3D). The timing of this glutamatergic signal could be shifted by changing the timing of visual feedback (Figures S4E and S4F). Notably, this glutamatic signal encoded the speed of visual input even without swimming (Figures 4G, 4H, and S4G). These results indicate that the gating of visually induced spiking by swimming (Figure 3F) arises from intrinsic mechanisms within the serotonergic neurons, rather than being inherited from upstream inputs to the DRN.

To identify the source of glutamatergic visual input into the raphe serotonergic neurons, we performed whole-brain imaging in swimming zebrafish under various visual input conditions (Figure S5). This analysis revealed six major brain areas that respond to visual feedback (Figures S5A–S5C). Canonical correlation analysis pointed to the thalamic area—a region directly innervated by retinal ganglion cells[39]—as a likely upstream source (Figures S5D and S5E). Axonal projections from the thalamus area overlap spatially with raphe dendrites, based on single-cell projection data[40] (Figure S5F). Visual responses were both delayed in the thalamus and raphe, contrasting with rapid responses in the optic tectum (Figures S5G and S5H), suggesting that the thalamus-raphe pathway transmits delayed visual feedback. Together with neurotransmitter imaging, these findings indicate that raphe serotonergic activity is shaped by local GABAergic inhibition and remote glutamatergic excitation from upstream visual areas.

To test whether the proposed mechanism can reproduce the key features observed in real neuronal data, we formulated a neural network model that simulates GABAergic neurons and serotonergic neurons in the raphe nucleus that receive swim and visually evoked inputs, respectively (Figures 5A and 5B). We also considered alternative models, but they were not consistent with the spiking and glutamate/GABA signals upon closer inspection (Figure S6). Based on the estimated response kernel derived from voltage imaging data (Figure 3E) and membrane potential dynamics following swim bouts in the absence of visual input (Figure S2E), which suggest the presence of post-inhibitory rebound, we included hyperpolarization-induced cation channels in the serotonergic neurons. We also implemented two streams of excitatory inputs into this neural network, including those triggered by swimming and those triggered by delayed visual feedback that differentially innervated raphe GABAergic neurons and serotonergic neurons, respectively. Simulating this system as a spiking neural network driven by swimming and visual motion (Figure 5C) generated time series of membrane potential and spiking activity (Figures 5D and 5E) that can be compared with the experimental data.

This model reproduced the spiking patterns and the encoding of swim-induced visual feedback, proportional to G_{ms}, from experimental data (Figure 5F). When we removed GABAergic neurons from the model, spiking responses to visual feedback were obliterated in serotonergic neurons due to the loss of post-inhibitory rebound. This result qualitatively matches the absence of visual spiking responses without swimming in replay experiments (Figures 5G and 5H). Further inspection of the model indicated that coincidence detection generally occurs in the low firing rate regime of the model parameters (Figures S7A and S7B), consistent with the observed firing rates in raphe serotonergic neurons. Taken together, the spiking network model and its recapitulation of experimental data support the action-outcome computation via the synergetic effects of swimming-evoked, post-inhibitory rebound and visually evoked glutamatergic input in serotonergic neurons, which ensures robust encoding of action effectiveness.

GABAergic inhibition enables the encoding of action effectiveness in serotonergic neurons

Serotonergic neurons in the DRN receive inhibitory input from local GABAergic neurons.[41,42] In zebrafish, raphe GABAergic neurons are known to encode the vigor of swimming[17] and likely contribute to the swim-evoked inhibition and, thereby, post-inhibitory rebound of serotonergic neurons (Figure 3). This process may provide the time window for visual input to evoke spiking in serotonergic neurons (Figure 6A).

We therefore investigated whether targeted ablation of raphe GABAergic neurons impairs the encoding of visual feedback

Please cite this article in press as: Kawashima et al., Voltage imaging reveals circuit computations in the raphe underlying serotonin-mediated motor vigor learning, Neuron (2025), https://doi.org/10.1016/j.neuron.2025.05.017

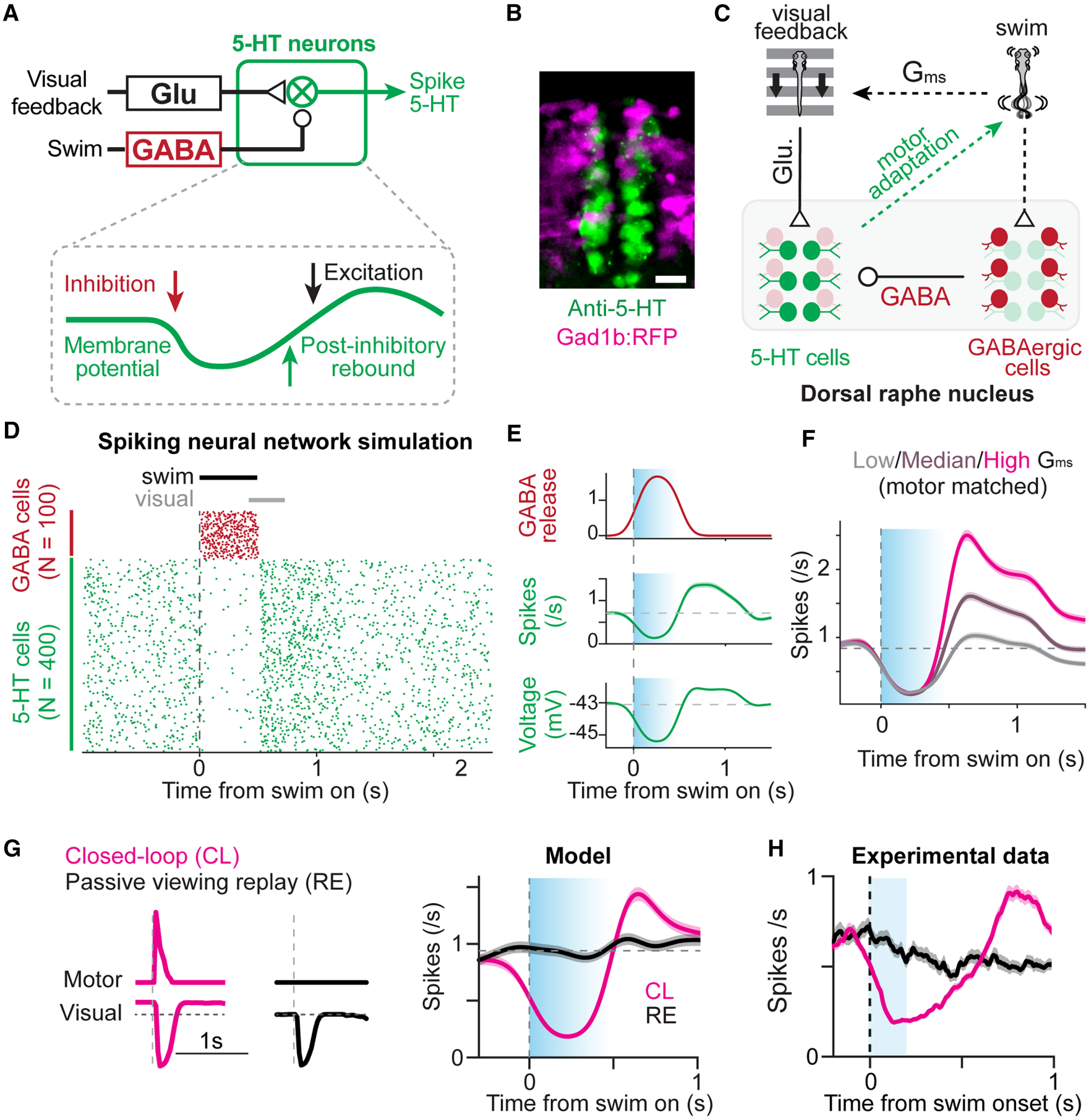

Figure 5. Simulation of sensory-motor integration in the serotonergic raphe using a spiking neural network

(A and B) (A) Model schematic of GABAergic input, glutamatergic input, post-inhibitory rebound, and spike/5-HT output in serotonergic neurons, and (B) matching anatomy showing serotonergic (green) and GABAergic neurons (red) in the raphe nucleus, which are largely non-overlapping populations in larval zebrafish. Scale bar, 10 μm.

(C) Structure of spiking neural network model.

(D) Simulated spiking activity during a single swim bout.

(E) Resulting GABA signals, 5-HT neuron spiking, and membrane potential in the model during a swim bout. Shading represents SEM across *n* = 100 GABA cells, *n* = 400 5-HT cells, and *n* = 400 5-HT cells respectively.

(F) The model shows during-swim suppression and post-swim visual response in serotonergic neurons, which recapitulates experimental results in Figure 3D. Shading represents SEM across *n* = 400 5-HT cells.

(G and H) The simulated serotonergic neurons do not show visual responses without motor-induced GABAergic inhibition (G), which matches the experimental data (H) replotted from Figure 3F. Shading represents SEM across cells. See also Figures S6 and S7.

during swimming in serotonergic neurons and affects motor adaptation behavior (Figure 6). We used two-photon plasma ablation[43] of raphe GABAergic neurons that express red fluorescence proteins[44] (Figure 6B). We performed voltage imaging in serotonergic neurons before and after the ablation to examine how the ablation affects their membrane potential modulation and spiking activity during motor adaptation. The ablation of raphe GABAergic neurons did not alter the spike shapes of serotonergic neurons, indicating minimal collateral damage (Figure 6C). As a control, we also performed ablations of GABAergic neurons outside the raphe (Figures S8A and S8B). We found that the ablation of a subset of raphe GABAergic neurons led to a reduction of inhibition during

Please cite this article in press as: Kawashima et al., Voltage imaging reveals circuit computations in the raphe underlying serotonin-mediated motor vigor learning, Neuron (2025), https://doi.org/10.1016/j.neuron.2025.05.017

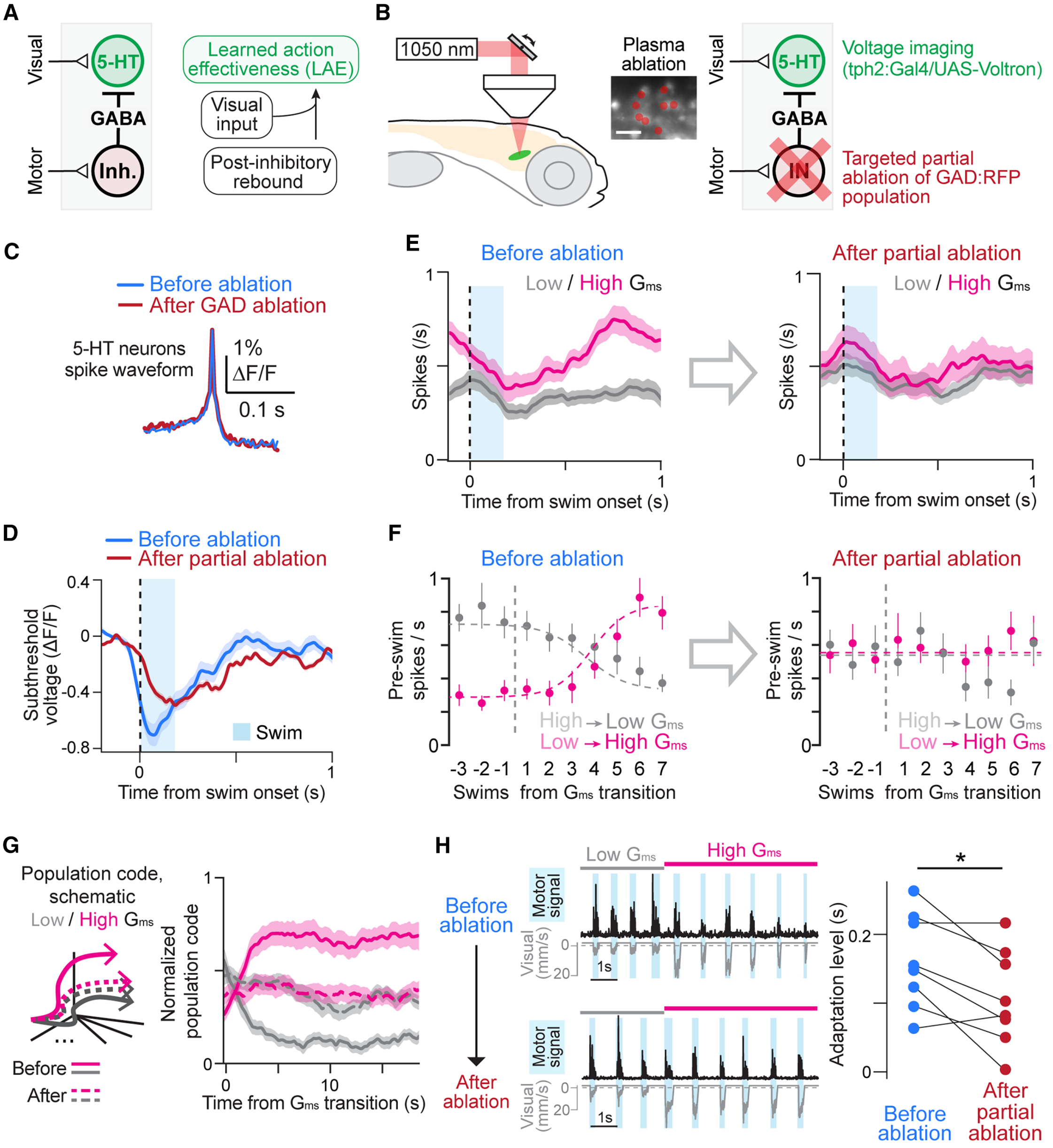

Figure 6. GABAergic neuron ablation impairs DRN motor-gating and population coding

(A) Hypothetical circuit diagram and learning mechanisms in the raphe nucleus.

(B) Two-photon plasma ablation of a subset of raphe GABAergic neurons that express red fluorescent protein (RFP, center). The loci of the ablation and control ablation are shown in Figures S8A and S8B. Voltage imaging in *tph2*+ neurons was performed before and after the ablation. Scale bar, 10 μm.

(C) Spike waveform in a representative serotonergic neuron remained intact after the ablation.

(D) Changes of membrane potential dynamics during swimming in serotonergic neurons before and after the GABAergic neuron ablation. The ablation decreased swimming-evoked inhibition as well as post-inhibitory rebound. *N* = 9 fish; 48 high-G_{ms} neurons; shading represents SEM across cells.

(E) The ablation resulted in the loss of visual responses in serotonergic neurons while their baseline firing remained intact. Spiking in serotonergic neurons before (left) and after (right) the ablation during low (gray) and high (magenta) G_{ms}. Data from 48 high-G_{ms} neurons in 9 fish; shading represents SEM across cells.

(F) The ablation impaired the slow changes in baseline firing rates in DRN serotonergic neurons, which were measured in a time window (100 ms) before each swim event and depicted as a function of swim number relative to G_{ms} transitions. Magenta and gray represent the transition from low to high G_{ms} and from high to low G_{ms}, respectively. *N* = 9 fish, 48 high-G_{ms}-preferring cells; error bars represent SEM across cells.

(G) The GABAergic neuron ablation impaired population coding of LAE in serotonergic neurons. Left: schematic of population coding for G_{ms}. Linear discriminant analysis based on spiking activity was performed to maximally separate trajectories between low vs. high G_{ms} (see STAR Methods). Right: while the 5-HT

(legend continued on next page)

Please cite this article in press as: Kawashima et al., Voltage imaging reveals circuit computations in the raphe underlying serotonin-mediated motor vigor learning, Neuron (2025), https://doi.org/10.1016/j.neuron.2025.05.017

swimming and subsequent post-inhibitory rebound in serotonergic neurons (Figure 6D). The swim-triggered hyperpolarization was not completely removed, possibly because of additional inhibitory sources outside of the raphe. Such significant reduction was not observed after the control ablation (Figure S8C), indicating that the raphe GABAergic neurons mainly contribute to swim-evoked inhibition and post-inhibitory rebound in serotonergic neurons.

Importantly, we found that the visually evoked increase in spike rate in the post-swim period was abolished after the ablation (Figure 6E), suggesting that the post-inhibitory rebound in serotonergic neurons induced by local GABAergic neurons is crucial for integrating visually driven excitatory inputs. Such changes were also partially observed in the control ablation (Figure S8D), which suggests that GABAergic neurons outside the raphe may also weakly modulate raphe serotonergic neurons. The ablation of raphe GABAergic neurons also abolished the gradual increase/decrease of base firing rates after the transition of motosensory gains (Figure 6F) and the loss of population encoding of LAE (Figure 6G), both of which were not observed in the control ablation (Figures S8E and S8F). These results indicate that the coincidence-detection mechanism in the serotonergic neurons is also crucial for the slow modulation of their tonic firing rates on longer timescales that mediate short-term motor learning.[17]

We also observed the partial impairment of motor vigor learning after the ablation of raphe GABAergic neurons (Figures 6H and S8G), which was not observed after the control ablation (Figure S8H). Taken together, these results indicate that GABAergic inhibition of serotonergic neurons is core to the learning of action effectiveness in the serotonergic system and that such neural circuit motifs may have broader implications for how the serotonergic system integrates multiple streams of information to control behavior in vertebrate species.

DISCUSSION

The inner workings of the serotonergic system[45,46] have remained underexplored, despite the involvement of the serotonergic system in a wide range of brain functions, including sensory responsiveness,[47,48] sleep regulation,[49] motor learning and planning,[15,16,50–52] mood regulation,[21,53,54] and shifts between interoception and exteroception.[55,56] The precise multimodal measurements of dendritic inputs, somatic voltage dynamics, and neuromodulatory outputs reported here provide a rare view into the inner circuit and biophysical workings of the vertebrate serotonergic raphe during flexible behavior.

Understanding neural computation involves identifying the input-output properties of the involved neurons. This question can be especially hard to address in nuclei such as the serotonergic raphe, in part because it is hard to access its cell-type-specific populations in a small nucleus deep beneath the cortex, where most of the recordings in mammals were done through electrophysiology[57,58] or fiber photometry.[54,59,60] Due to the development of modern imaging sensors[61,62] and whole-brain imaging technology,[63–66] we were able to record multiple types of neuronal signals in the zebrafish raphe that are normally difficult to access. Our study provides a systematic way to track upstream inputs, local computation, and downstream outputs of the serotonergic system using multimodal imaging. These signals show dynamics inside the DRN that underlie the computation of action effectiveness, and suggest that neuromodulation arises from precise, fast-timescale, cellular and circuit mechanisms, and that the nuclei themselves implement these computations rather than simply inherit them from upstream input.

Motor learning relies on an animal's ability to identify the causal outcomes of its actions amidst numerous streams of ongoing sensory input, and temporal coincidence detection can facilitate this process. Coincidence-detection mechanisms have been reported across various domains within neuroscience, such as in dendritic integration,[67] synaptic plasticity,[68] and sensory processing.[69] Synergetic effects of post-inhibitory rebound with excitatory inputs have been proposed as a coincidence-detection mechanism in auditory processing[70,71] and associative learning.[72] Our study provides evidence that this type of coincidence detection mediates robust encoding of action effectiveness for motor learning. At the subcellular level, this coincidence-detection mechanism likely occurs in the dendrites of serotonergic neurons. Post-inhibitory rebound occurs in dendrites,[73,74] and we observed GABAergic and glutamatergic inputs in dendrites. This could explain the lack of significant increase in membrane potential in the soma during the open-loop replay trials without swimming despite the presence of visually driven glutamatergic inputs. With more sensitive voltage reporters measured at the dendrites in the future, the question of localized interactions with glutamatergic input and post-inhibitory rebound can be elucidated at these finer scales. The use of temporal coincidence between post-inhibitory rebound and excitatory input, rather than an arguably simpler coincidence of two excitatory inputs,[75] may have the advantage of inhibiting serotonergic neurons when there is no sensory feedback from motor actions. Indeed, in reinforcement learning, midbrain dopamine neurons show suppression of firing rates when rewards are not given at expected times,[76] which is partially mediated by inhibitory inputs from local GABAergic neurons.[57] Thus, such bidirectional control of firing rates in monoaminergic neurons may be necessary for flexible control of behavioral states.

The cellular interactions underlying the gating of sensory processing during motor vigor learning uncovered in this study provide evidence for specific cellular properties and network connectivity structure. Proving their existence is a topic for future studies. First, the presence of hyperpolarization-activated channels necessary for post-inhibitory rebound in serotonergic neurons can be verified using single-cell RNA sequencing and whole-cell recordings. Second, the connectivity structure between neurons conveying visual and motor signals to the DRN through glutamatergic and GABAergic connections, as well as

---

neuronal population code reliably distinguished low from high G_{ms} (solid gray and magenta lines) before the ablation, this population code disappeared after the ablation (dashed lines). $N = 8$ fish, 15 sessions, 10–20 cells simultaneously recorded per session; shading represents SEM across sessions.

(H) The ablation of DRN GABAergic neurons leads to a reduction in motor adaptation. We measured the number of time points within swim signals with statistical differences between low vs. high G_{ms} (see STAR Methods). $N = 8$ fish. $^{*}p = 0.0277$, paired signed-rank test. See also Figure S8.

the identities of these upstream neurons, can be verified using connectomics or viral tracing. Third, improvements in imaging resolution and synaptic specificity of glutamate and GABA sensors will elucidate which spatial aspects of the observed neurotransmitter release mediate dendritic computations in serotonergic neurons. Immunohistochemistry, in combination with subcellular markers, can be used to quantify the relevant receptor distribution along these dendrites. Finally, the mechanisms linking different timescales in serotonergic neurons, enabling fast phasic activity to drive slow modulation of tonic firing, remain to be identified. Connectomics or other tracing and receptor-identification methods will elucidate the network structure underlying persistent activity in the DRN that integrates the motor-gated visual signals over time.

The serotonergic system controls various brain states,[21,22,49–51,59,77–82] yet its internal computational principles require clarification. We propose that the computational motif that enables action-outcome computation in the serotonergic system in zebrafish may generalize to computations that trigger other brain state transitions. For example, action effectiveness can reflect levels of challenge in a variety of situations, including in learned-helplessness contexts.[16,82,83] Our study indicates that 5-HT levels decrease as a function of the difficulty of the task. The input-output transform within the serotonergic system may thus reflect an internal "credit system" for the outcomes of actions, which may be related to reward encoding in the serotonergic system,[18,20] or, more generally, the encoding of the overall level of challenge or perseverance required in broader behavioral contexts.[22,81] Action effectiveness within the zebrafish motor learning model relates, conceptually, to self-efficacy in human psychology, defined as one's belief in one's capacity to act in the ways necessary to reach specific goals.[84,85]

We have formulated a motor learning framework based on the concept of LAE. This computational framework effectively accounts for motor learning at the behavioral level, 5-HT release dynamics, and population coding in the serotonergic system during short-term motor learning, and enabled the construction of a spiking neural network model accounting for the activity of multiple neuronal types. Our findings highlight that serotonergic neuromodulation relies on fast, precise circuit computations within the raphe, such as action-outcome coincidence detection, to control behavioral adaptation. This suggests that similarly intricate mechanisms may operate across other neuromodulatory nuclei. Further exploration of cellular and circuit dynamics within these nuclei during behavior in multiple species will deepen our understanding of the common principles underlying the dynamic regulation of brain states by different neuromodulatory systems.

RESOURCE AVAILABILITY

Lead contact

Further information and requests for resources should be directed to and will be fulfilled by the lead contact, Misha B. Ahrens (ahrensm@janelia.hhmi.org).

Materials availability

Tg(elavl3:iSeroSnFR) is available from the Kawashima laboratory upon request. Other fish lines generated in this study are available from the lead contact without restriction.

Data and code availability

- Processed data have been deposited at Mendeley Data and are publicly available as of the date of publication at Mendeley Data: https://doi.org/10.17632/3nn5t35j8s. Raw microscopy imaging data reported in this paper will be shared by the lead contact upon request.
- Microscope control software used for 5-HT imaging was deposited at Zenodo at https://doi.org/10.5281/zenodo.15301729. Original code for processing voltage imaging data was deposited at Zenodo at https://doi.org/10.5281/zenodo.15293026. Original code for data analyses has been deposited at Zenodo at https://doi.org/10.5281/zenodo.15293043. All code is publicly available as of the date of publication.
- Any additional information required to reanalyze the data reported in this work paper is available from the lead contact upon request.

ACKNOWLEDGMENTS

We thank Carsen Stringer, Yu Mu, Florian Engert, Sandro Romani, Brett Mensh, and David Prober for their comments on the manuscript. We thank Liam Paninski for the discussions on data analysis. We thank Adam Cohen, Brett Mensh, and members from the Ahrens lab and Kawashima lab for discussions on this project. This project was funded by the Howard Hughes Medical Institute (M.B.A.), the Simons Foundation Simons Collaboration on the Global Brain Award 542943SPI (M.B.A.), the Israel Science Foundation Individual Grant 688/22 (T.K.), the Binational Science Foundation #2021746 (T.K.), an Azrieli faculty fellowship (T.K.), an Abisch Frenkel Foundation (T.K.), Jonathan and Joan Birnbach (T.K.), Dan Lebas & Ruth Sonnewend (T.K.), an internal grant from the Center for New Scientists at Weizmann Institute of Science (T.K.), the Janelia Visiting Scientist Program (T.K.), the Israeli Council for Higher Education (CHE) via the Weizmann Data Science Research Center (R.H.), the Moshe Meir Horwitz Fund (R.H.), the Max Planck Society (H.B.), the Bridge Position Program for Advancing Women in Science and Gender Equality in Weizmann Institute of Science (I.S.), and an Alexander von Humboldt postdoctoral fellowship (I.S.).

AUTHOR CONTRIBUTIONS

T.K. conceived of the project; performed experiments on motor adaptation behavior, voltage imaging, neurotransmitter imaging, and two-photon plasma ablation; performed data analysis; and wrote the manuscript. Z.W. conceived of the project, developed data processing pipelines for voltage imaging and neurotransmitter imaging, performed data analysis and modeling, and wrote the manuscript. R.H. generated transgenic zebrafish and performed the 5-HT imaging experiment. S.N. generated transgenic zebrafish for voltage and neurotransmitter imaging. I.S. and H.B. generated transgenic zebrafish for 5-HT imaging. M.B.A. conceived of and supervised this study, analyzed data, and wrote the manuscript.

DECLARATION OF INTERESTS

The authors declare no competing interests.

STAR★METHODS

Detailed methods are provided in the online version of this paper and include the following:

- KEY RESOURCES TABLE
- EXPERIMENTAL MODEL AND STUDY PARTICIPANT DETAILS
  - Zebrafish husbandry
  - Transgenic zebrafish
- METHOD DETAILS
  - Preparation for zebrafish imaging experiments
  - Light-sheet imaging
  - Behavioral Assays in Virtual Reality
  - Behavioral tasks

SUPPLEMENTAL INFORMATION

Supplemental information can be found online at https://doi.org/10.1016/j.neuron.2025.05.017.

Received: September 16, 2024
Revised: March 4, 2025
Accepted: May 14, 2025

REFERENCES

1. Flavell, S.W., Gogolla, N., Lovett-Barron, M., and Zelikowsky, M. (2022). The emergence and influence of internal states. Neuron *110*, 2545–2570. https://doi.org/10.1016/j.neuron.2022.04.030.
2. Harris-Warrick, R.M., and Marder, E. (1991). Modulation of Neural Networks for Behavior. Annu. Rev. Neurosci. *14*, 39–57. https://doi.org/10.1146/annurev.ne.14.030191.000351.
3. Lefton, K.B., Wu, Y., Dai, Y., Okuda, T., Zhang, Y., Yen, A., Rurak, G.M., Walsh, S., Manno, R., Myagmar, B.E., Dougherty, J.D., Samineni, V.K., et al. (2025). Norepinephrine Signals Through Astrocytes To Modulate Synapses. Science *388*, 776–783. https://doi.org/10.1126/science.adq5480.
4. Dayan, P., and Huys, Q. (2015). Serotonin's many meanings elude simple theories. eLife *4*, e07390. https://doi.org/10.7554/eLife.07390.
5. Ahrens, M.B., Li, J.M., Orger, M.B., Robson, D.N., Schier, A.F., Engert, F., and Portugues, R. (2012). Brain-wide neuronal dynamics during motor adaptation in zebrafish. Nature *485*, 471–477. https://doi.org/10.1038/nature11057.
6. Portugues, R., and Engert, F. (2011). Adaptive locomotor behavior in larval zebrafish. Front. Syst. Neurosci. *5*, 72. https://doi.org/10.3389/fnsys.2011.00072.
7. Yang, E., Zwart, M.F., James, B., Rubinov, M., Wei, Z., Narayan, S., Vladimirov, N., Mensh, B.D., Fitzgerald, J.E., and Ahrens, M.B. (2022). A brainstem integrator for self-location memory and positional homeostasis in zebrafish. Cell *185*, 5011–5027.e20. https://doi.org/10.1016/j.cell.2022.11.022.
8. Alexander, G.E., DeLong, M.R., and Strick, P.L. (1986). Parallel organization of functionally segregated circuits linking basal ganglia and cortex. Annu. Rev. Neurosci. *9*, 357–381. https://doi.org/10.1146/annurev.ne.09.030186.002041.
9. Makino, H., Ren, C., Liu, H., Kim, A.N., Kondapaneni, N., Liu, X., Kuzum, D., and Komiyama, T. (2017). Transformation of Cortex-wide Emergent Properties during Motor Learning. Neuron *94*, 880–890.e8. https://doi.org/10.1016/j.neuron.2017.04.015.
10. Wolpert, D.M., Miall, R.C., and Kawato, M. (1998). Internal models in the cerebellum. Trends Cogn. Sci. *2*, 338–347. https://doi.org/10.1016/S1364-6613(98)01221-2.
11. da Silva, J.A., Tecuapetla, F., Paixão, V., and Costa, R.M. (2018). Dopamine neuron activity before action initiation gates and invigorates future movements. Nature *554*, 244–248. https://doi.org/10.1038/nature25457.
12. Jacobs, B.L., and Fornal, C.A. (1997). Serotonin and motor activity. Curr. Opin. Neurobiol. *7*, 820–825. https://doi.org/10.1016/s0959-4388(97)80141-9.
13. Yttri, E.A., and Dudman, J.T. (2016). Opponent and bidirectional control of movement velocity in the basal ganglia. Nature *533*, 402–406. https://doi.org/10.1038/nature17639.
14. Perrier, J.-F., Rasmussen, H.B., Jørgensen, L.K., and Berg, R.W. (2017). Intense Activity of the Raphe Spinal Pathway Depresses Motor Activity via a Serotonin Dependent Mechanism. Front. Neural Circuits *11*, 111. https://doi.org/10.3389/fncir.2017.00111.
15. Correia, P.A., Lottem, E., Banerjee, D., Machado, A.S., Carey, M.R., and Mainen, Z.F. (2017). Transient inhibition and long-term facilitation of locomotion by phasic optogenetic activation of serotonin neurons. eLife *6*, e20975. https://doi.org/10.7554/eLife.20975.
16. Seo, C., Guru, A., Jin, M., Ito, B., Sleezer, B.J., Ho, Y.-Y., Wang, E., Boada, C., Krupa, N.A., Kullakanda, D.S., et al. (2019). Intense threat switches dorsal raphe serotonin neurons to a paradoxical operational mode. Science *363*, 538–542. https://doi.org/10.1126/science.aau8722.
17. Kawashima, T., Zwart, M.F., Yang, C.-T., Mensh, B.D., and Ahrens, M.B. (2016). The serotonergic system tracks the outcomes of actions to mediate short-term motor learning. Cell *167*, 933–946.e20. https://doi.org/10.1016/j.cell.2016.09.055.
18. Cohen, J.Y., Amoroso, M.W., and Uchida, N. (2015). Serotonergic neurons signal reward and punishment on multiple timescales. eLife *4*, e06346. https://doi.org/10.7554/eLife.06346.
19. Harkin, E.F., Grossman, C.D., Cohen, J.Y., Béïque, J.-C., and Naud, R. (2025). A prospective code for value in the serotonergic system. Nature *641*, 952–959. https://doi.org/10.1038/s41586-025-08731-7.
20. Liu, Z., Zhou, J., Li, Y., Hu, F., Lu, Y., Ma, M., Feng, Q., Zhang, J.E., Wang, D., Zeng, J., et al. (2014). Dorsal Raphe Neurons Signal Reward through 5-HT and Glutamate. Neuron *81*, 1360–1374. https://doi.org/10.1016/j.neuron.2014.02.010.
21. Marcinkiewcz, C.A., Mazzone, C.M., D'Agostino, G., Halladay, L.R., Hardaway, J.A., DiBerto, J.F., Navarro, M., Burnham, N., Cristiano, C., Dorrier, C.E., et al. (2016). Serotonin engages an anxiety and fear-promoting circuit in the extended amygdala. Nature *537*, 97–101. https://doi.org/10.1038/nature19318.
22. Marques, J.C., Li, M., Schaak, D., Robson, D.N., and Li, J.M. (2020). Internal state dynamics shape brainwide activity and foraging behaviour. Nature *577*, 239–243. https://doi.org/10.1038/s41586-019-1858-z.
23. Ren, J., Isakova, A., Friedmann, D., Zeng, J., Grutzner, S.M., Pun, A., Zhao, G.Q., Kolluru, S.S., Wang, R., Lin, R., et al. (2019). Single-cell transcriptomes and whole-brain projections of serotonin neurons in the mouse dorsal and median raphe nuclei. eLife *8*, e49424. https://doi.org/10.7554/eLife.49424.
24. Haruvi, R., Barbara, R., Shainer, I., Rosenberg, A., Moshe, L., Malamud, D., Toledano, J., Braun, D., Baier, H., and Kawashima, T. (2024). Global and compartmentalized serotonergic control of sensorimotor integration underlying motor adaptation. Preprint at bioRxiv. https://doi.org/10.1101/2024.09.15.613094.
25. Unger, E.K., Keller, J.P., Altermatt, M., Liang, R., Matsui, A., Dong, C., Hon, O.J., Yao, Z., Sun, J., Banala, S., et al. (2020). Directed Evolution of a Selective and Sensitive Serotonin Sensor via Machine Learning. Cell *183*, 1986–2002.e26. https://doi.org/10.1016/j.cell.2020.11.040.
26. Abdelfattah, A.S., Kawashima, T., Singh, A., Novak, O., Liu, H., Shuai, Y., Huang, Y.-C., Campagnola, L., Seeman, S.C., Yu, J., et al. (2019). Bright and photostable chemigenetic indicators for extended in vivo voltage imaging. Science *365*, 699–704. https://doi.org/10.1126/science.aav6416.
27. Wei, Z., Lin, B.-J., Chen, T.-W., Daie, K., Svoboda, K., and Druckmann, S. (2020). A comparison of neuronal population dynamics measured with calcium imaging and electrophysiology. PLoS Comput. Biol. *16*, e1008198. https://doi.org/10.1371/journal.pcbi.1008198.
28. Vandermaelen, C.P., and Aghajanian, G.K. (1983). Electrophysiological and pharmacological characterization of serotonergic dorsal raphe neurons recorded extracellularly and intracellularly in rat brain slices. Brain Res. *289*, 109–119. https://doi.org/10.1016/0006-8993(83)90011-2.

29. Burlhis, T.M., and Aghajanian, G.K. (1987). Pacemaker potentials of serotonergic dorsal raphe neurons: contribution of a low-threshold Ca2+ conductance. Synapse *1*, 582–588. https://doi.org/10.1002/syn.890010611.

30. Angstadt, J.D., Grassmann, J.L., Theriault, K.M., and Levasseur, S.M. (2005). Mechanisms of postinhibitory rebound and its modulation by serotonin in excitatory swim motor neurons of the medicinal leech. J. Comp. Physiol. A Neuroethol. Sens. Neural Behav. Physiol. *191*, 715–732. https://doi.org/10.1007/s00359-005-0628-6.

31. Goaillard, J.-M., Taylor, A.L., Pulver, S.R., and Marder, E. (2010). Slow and Persistent Postinhibitory Rebound Acts as an Intrinsic Short-Term Memory Mechanism. J. Neurosci. *30*, 4687–4692. https://doi.org/10.1523/JNEUROSCI.2998-09.2010.

32. Zhao, Y., Huang, C.-X., Gu, Y., Zhao, Y., Ren, W., Wang, Y., Chen, J., Guan, N.N., and Song, J. (2024). Serotonergic modulation of vigilance states in zebrafish and mice. Nat. Commun. *15*, 2596. https://doi.org/10.1038/s41467-024-47021-0.

33. Zheng, N., and Raman, I.M. (2011). Prolonged postinhibitory rebound firing in the cerebellar nuclei mediated by group I metabotropic glutamate receptor potentiation of L-type calcium currents. J. Neurosci. *31*, 10283–10292. https://doi.org/10.1523/JNEUROSCI.1834-11.2011.

34. Tao, R., and Auerbach, S.B. (2000). Regulation of serotonin release by GABA and excitatory amino acids. J. Psychopharmacol. *14*, 100–113. https://doi.org/10.1177/026988110001400201.

35. Weissbourd, B., Ren, J., DeLoach, K.E., Guenthner, C.J., Miyamichi, K., and Luo, L. (2014). Presynaptic partners of dorsal raphe serotonergic and GABAergic neurons. Neuron *83*, 645–662. https://doi.org/10.1016/j.neuron.2014.06.024.

36. Marvin, J.S., Shimoda, Y., Magloire, V., Leite, M., Kawashima, T., Jensen, T.P., Kolb, I., Knott, E.L., Novak, O., Podgorski, K., et al. (2019). A genetically encoded fluorescent sensor for in vivo imaging of GABA. Nat. Methods *16*, 763–770. https://doi.org/10.1038/s41592-019-0471-2.

37. Marvin, J.S., Scholl, B., Wilson, D.E., Podgorski, K., Kazemipour, A., Müller, J.A., Schoch, S., Quiroz, F.J.U., Rebola, N., Bao, H., et al. (2018). Stability, affinity, and chromatic variants of the glutamate sensor iGluSnFR. Nat. Methods *15*, 936–939. https://doi.org/10.1038/s41592-018-0171-3.

38. Liu, R., Jolas, T., and Aghajanian, G. (2000). Serotonin 5-HT$_2$ receptors activate local GABA inhibitory inputs to serotonergic neurons of the dorsal raphe nucleus. Brain Res. *873*, 34–45. https://doi.org/10.1016/S0006-8993(00)02468-9.

39. Baier, H., and Wullimann, M.F. (2021). Anatomy and function of retinorecipient arborization fields in zebrafish. J. Comp. Neurol. *529*, 3454–3476. https://doi.org/10.1002/cne.25204.

40. Kunst, M., Laurell, E., Mokayes, N., Kramer, A., Kubo, F., Fernandes, A.M., Förster, D., Dal Maschio, M., and Baier, H. (2019). A Cellular-Resolution Atlas of the Larval Zebrafish Brain. Neuron *103*, 21–38.e5. https://doi.org/10.1016/j.neuron.2019.04.034.

41. Hernández-Vázquez, F., Garduño, J., and Hernández-López, S. (2019). GABAergic modulation of serotonergic neurons in the dorsal raphe nucleus. Rev. Neurosci. *30*, 289–303. https://doi.org/10.1515/revneuro-2018-0014.

42. Soiza-Reilly, M., and Commons, K.G. (2014). Unraveling the architecture of the dorsal raphe synaptic neuropil using high-resolution neuroanatomy. Front. Neural Circuits *8*, 105. https://doi.org/10.3389/fncir.2014.00105.

43. Tsai, P.S., Blinder, P., Migliori, B.J., Neev, J., Jin, Y., Squier, J.A., and Kleinfeld, D. (2009). Plasma-mediated ablation: an optical tool for submicrometer surgery on neuronal and vascular systems. Curr. Opin. Biotechnol. *20*, 90–99. https://doi.org/10.1016/j.copbio.2009.02.003.

44. Satou, C., Kimura, Y., Hirata, H., Suster, M.L., Kawakami, K., and Higashijima, S. (2013). Transgenic tools to characterize neuronal properties of discrete populations of zebrafish neurons. Development *140*, 3927–3931. https://doi.org/10.1242/dev.099531.

45. Huang, K.W., Ochandarena, N.E., Philson, A.C., Hyun, M., Birnbaum, J.E., Cicconet, M., and Sabatini, B.L. (2019). Molecular and anatomical organization of the dorsal raphe nucleus. eLife *8*, e46464. https://doi.org/10.7554/eLife.46464.

46. Ren, J., Friedmann, D., Xiong, J., Liu, C.D., Ferguson, B.R., Weerakkody, T., DeLoach, K.E., Ran, C., Pun, A., Sun, Y., et al. (2018). Anatomically Defined and Functionally Distinct Dorsal Raphe Serotonin Sub-systems. Cell *175*, 472–487.e20. https://doi.org/10.1016/j.cell.2018.07.043.

47. Kapoor, V., Provost, A.C., Agarwal, P., and Murthy, V.N. (2016). Activation of raphe nuclei triggers rapid and distinct effects on parallel olfactory bulb output channels. Nat. Neurosci. *19*, 271–282. https://doi.org/10.1038/nn.4219.

48. Yokogawa, T., Hannan, M.C., and Burgess, H.A. (2012). The dorsal raphe modulates sensory responsiveness during arousal in zebrafish. J. Neurosci. *32*, 15205–15215. https://doi.org/10.1523/JNEUROSCI.1019-12.2012.

49. Oikonomou, G., Altermatt, M., Zhang, R.-W., Coughlin, G.M., Montz, C., Gradinaru, V., and Prober, D.A. (2019). The Serotonergic Raphe Promote Sleep in Zebrafish and Mice. Neuron *103*, 686–701.e8. https://doi.org/10.1016/j.neuron.2019.05.038.

50. Fonseca, M.S., Murakami, M., and Mainen, Z.F. (2015). Activation of dorsal raphe serotonergic neurons promotes waiting but is not reinforcing. Curr. Biol. *25*, 306–315. https://doi.org/10.1016/j.cub.2014.12.002.

51. Miyazaki, K.W., Miyazaki, K., Tanaka, K.F., Yamanaka, A., Takahashi, A., Tabuchi, S., and Doya, K. (2014). Optogenetic activation of dorsal raphe serotonin neurons enhances patience for future rewards. Curr. Biol. *24*, 2033–2040. https://doi.org/10.1016/j.cub.2014.07.041.

52. Soubrié, P. (1986). Reconciling the role of central serotonin neurons in human and animal behavior. Behav. Brain Sci. *9*, 319–335. https://doi.org/10.1017/S0140525X00022871.

53. Matthews, P.R., and Harrison, P.J. (2012). A morphometric, immunohistochemical, and in situ hybridization study of the dorsal raphe nucleus in major depression, bipolar disorder, schizophrenia, and suicide. J. Affect. Disord. *137*, 125–134. https://doi.org/10.1016/j.jad.2011.10.043.

54. Paquelet, G.E., Carrion, K., Lacefield, C.O., Zhou, P., Hen, R., and Miller, B.R. (2022). Single-cell activity and network properties of dorsal raphe nucleus serotonin neurons during emotionally salient behaviors. Neuron *110*, 2664–2679.e8. https://doi.org/10.1016/j.neuron.2022.05.015.

55. Burrows, K., DeVille, D.C., Cosgrove, K.T., Kuplicki, R.T., Tulsa 1000 Investigators, Paulus, M.P., Aupperle, R., Khalsa, S.S., and Stewart, J.L. (2022). Impact of serotonergic medication on interoception in major depressive disorder. Biol. Psychol. *169*, 108286. https://doi.org/10.1016/j.biopsycho.2022.108286.

56. Livermore, J.J.A., Holmes, C.L., Moga, G., Adamatzky, K., Critchley, H.D., Garfinkel, S.N., and Campbell-Meiklejohn, D. (2022). A single oral dose of citalopram increases interoceptive insight in healthy volunteers. Psychopharmacology *239*, 2289–2298. https://doi.org/10.1007/s00213-022-06115-7.

57. Eshel, N., Bukwich, M., Rao, V., Hemmelder, V., Tian, J., and Uchida, N. (2015). Arithmetic and local circuitry underlying dopamine prediction errors. Nature *525*, 243–246. https://doi.org/10.1038/nature14855.

58. Cohen, J.Y., Haesler, S., Vong, L., Lowell, B.B., and Uchida, N. (2012). Neuron-type-specific signals for reward and punishment in the ventral tegmental area. Nature *482*, 85–88. https://doi.org/10.1038/nature10754.

59. Akbar, L., Castillo, V.C.G., Olorocisimo, J.P., Ohta, Y., Kawahara, M., Takehara, H., Haruta, M., Tashiro, H., Sasagawa, K., Ohsawa, M., et al. (2023). Multi-Region Microdialysis Imaging Platform Revealed Dorsal Raphe Nucleus Calcium Signaling and Serotonin Dynamics during

Please cite this article in press as: Kawashima et al., Voltage imaging reveals circuit computations in the raphe underlying serotonin-mediated motor vigor learning, Neuron (2025), https://doi.org/10.1016/j.neuron.2025.05.017

Nociceptive Pain. Int. J. Mol. Sci. *24*, 6654. https://doi.org/10.3390/ijms24076654.

60. Paquelet, G.E., Carrion, K., Lacefield, C.O., Zhou, P., Hen, R., and Miller, B.R. (2023). Protocol for in vivo imaging and analysis of brainstem neuronal activity in the dorsal raphe nucleus of freely behaving mice. Star Protoc. *4*, 102074. https://doi.org/10.1016/j.xpro.2023.102074.
61. Dong, C., Zheng, Y., Long-Iyer, K., Wright, E.C., Li, Y., and Tian, L. (2022). Fluorescence Imaging of Neural Activity, Neurochemical Dynamics, and Drug-Specific Receptor Conformation with Genetically Encoded Sensors. Annu. Rev. Neurosci. *45*, 273–294. https://doi.org/10.1146/annurev-neuro-110520-031137.
62. Wu, Z., Lin, D., and Li, Y. (2022). Pushing the frontiers: tools for monitoring neurotransmitters and neuromodulators. Nat. Rev. Neurosci. *23*, 257–274. https://doi.org/10.1038/s41583-022-00577-6.
63. Ahrens, M.B., Orger, M.B., Robson, D.N., Li, J.M., and Keller, P.J. (2013). Whole-brain functional imaging at cellular resolution using light-sheet microscopy. Nat. Methods *10*, 413–420. https://doi.org/10.1038/nmeth.2434.
64. Panier, T., Romano, S.A., Olive, R., Pietri, T., Sumbre, G., Candelier, R., and Debrégeas, G. (2013). Fast functional imaging of multiple brain regions in intact zebrafish larvae using Selective Plane Illumination Microscopy. Front. Neural Circuits *7*, 65. https://doi.org/10.3389/fncir.2013.00065.
65. Vladimirov, N., Mu, Y., Kawashima, T., Bennett, D.V., Yang, C.-T., Looger, L.L., Keller, P.J., Freeman, J., and Ahrens, M.B. (2014). Light-sheet functional imaging in fictively behaving zebrafish. Nat. Methods *11*, 883–884. https://doi.org/10.1038/nmeth.3040.
66. Barbara, R., Nagathihalli Kantharaju, M., Haruvi, R., Harrington, K., and Kawashima, T. (2022). PyZebrascope: An Open-Source Platform for Brain-Wide Neural Activity Imaging in Zebrafish. Front. Cell Dev. Biol. *10*, 875044. https://doi.org/10.3389/fcell.2022.875044.
67. Wang, S.S., Denk, W., and Häusser, M. (2000). Coincidence detection in single dendritic spines mediated by calcium release. Nat. Neurosci. *3*, 1266–1273. https://doi.org/10.1038/81792.
68. Egger, V., Feldmeyer, D., and Sakmann, B. (1999). Coincidence detection and changes of synaptic efficacy in spiny stellate neurons in rat barrel cortex. Nat. Neurosci. *2*, 1098–1105. https://doi.org/10.1038/16026.
69. König, P., Engel, A.K., and Singer, W. (1996). Integrator or coincidence detector? The role of the cortical neuron revisited. Trends Neurosci. *19*, 130–137. https://doi.org/10.1016/s0166-2236(96)80019-1.
70. Schöneich, S., Kostarakos, K., and Hedwig, B. (2015). An auditory feature detection circuit for sound pattern recognition. Sci. Adv. *1*, e1500325. https://doi.org/10.1126/sciadv.1500325.
71. Svirskis, G., Kotak, V., Sanes, D.H., and Rinzel, J. (2004). Sodium along with low-threshold potassium currents enhance coincidence detection of subthreshold noisy signals in MSO neurons. J. Neurophysiol. *91*, 2465–2473. https://doi.org/10.1152/jn.00717.2003.
72. Wetmore, D.Z., Mukamel, E.A., and Schnitzer, M.J. (2008). Lock-and-Key Mechanisms of Cerebellar Memory Recall Based on Rebound Currents. J. Neurophysiol. *100*, 2328–2347. https://doi.org/10.1152/jn.00344.2007.
73. Magee, J.C. (1998). Dendritic Hyperpolarization-Activated Currents Modify the Integrative Properties of Hippocampal CA1 Pyramidal Neurons. J. Neurosci. *18*, 7613–7624. https://doi.org/10.1523/JNEUROSCI.18-19-07613.1998.
74. Ascoli, G.A., Gasparini, S., Medinilla, V., and Migliore, M. (2010). Local Control of Postinhibitory Rebound Spiking in CA1 Pyramidal Neuron Dendrites. J. Neurosci. *30*, 6434–6442. https://doi.org/10.1523/JNEUROSCI.4066-09.2010.
75. Pena, J.L., Viete, S., Funabiki, K., Saberi, K., and Konishi, M. (2001). Cochlear and neural delays for coincidence detection in owls. J. Neurosci. *21*, 9455–9459. https://doi.org/10.1523/JNEUROSCI.21-23-09455.2001.
76. Schultz, W., Dayan, P., and Montague, P.R. (1997). A neural substrate of prediction and reward. Science *275*, 1593–1599. https://doi.org/10.1126/science.275.5306.1593.
77. Cazettes, F., Reato, D., Morais, J.P., Renart, A., and Mainen, Z.F. (2021). Phasic Activation of Dorsal Raphe Serotonergic Neurons Increases Pupil Size. Curr. Biol. *31*, 192–197.e4. https://doi.org/10.1016/j.cub.2020.09.090.
78. Choudhary, V., Heller, C.R., Aimon, S., de Sardenberg Schmid, L., Robson, D.N., and Li, J.M. (2023). Neural and behavioral organization of rapid eye movement sleep in zebrafish. Preprint at bioRxiv. https://doi.org/10.1101/2023.08.28.555077.
79. Deakin, J.F., and Graeff, F.G. (1991). 5-HT and mechanisms of defence. J. Psychopharmacol. *5*, 305–315. https://doi.org/10.1177/026988119100500414.
80. He, Y., Cai, X., Liu, H., Conde, K.M., Xu, P., Li, Y., Wang, C., Yu, M., He, Y., Liu, H., et al. (2021). 5-HT recruits distinct neurocircuits to inhibit hunger-driven and non-hunger-driven feeding. Mol. Psychiatry *26*, 7211–7224. https://doi.org/10.1038/s41380-021-01220-z.
81. Lottem, E., Banerjee, D., Vertechi, P., Sarra, D., Lohuis, M.O., and Mainen, Z.F. (2018). Activation of serotonin neurons promotes active persistence in a probabilistic foraging task. Nat. Commun. *9*, 1000. https://doi.org/10.1038/s41467-018-03438-y.
82. Maier, S.F. (1984). Learned helplessness and animal models of depression. Prog. Neuropsychopharmacol. Biol. Psychiatry *8*, 435–446. https://doi.org/10.1016/S0278-5846(84)80032-9.
83. Warden, M.R., Selimbeyoglu, A., Mirzabekov, J.J., Lo, M., Thompson, K.R., Kim, S.-Y., Adhikari, A., Tye, K.M., Frank, L.M., and Deisseroth, K. (2012). A prefrontal cortex-brainstem neuronal projection that controls response to behavioural challenge. Nature *492*, 428–432. https://doi.org/10.1038/nature11617.
84. Bandura, A. (1977). Self-efficacy: Toward a unifying theory of behavioral change. Psychol. Rev. *84*, 191–215. https://doi.org/10.1037//0033-295x.84.2.191.
85. Bandura, A. (1997). Self-Efficacy: the Exercise of Control (Macmillan).
86. Dunn, T.W., Mu, Y., Narayan, S., Randlett, O., Naumann, E.A., Yang, C.T., Schier, A.F., Freeman, J., Engert, F., and Ahrens, M.B. (2016). Brain-wide mapping of neural activity controlling zebrafish exploratory locomotion. eLife *5*, e12741. https://doi.org/10.7554/eLife.12741.
87. White, R.M., Sessa, A., Burke, C., Bowman, T., LeBlanc, J., Ceol, C., Bourque, C., Dovey, M., Goessling, W., Burns, C.E., et al. (2008). Transparent adult zebrafish as a tool for in vivo transplantation analysis. Cell Stem Cell *2*, 183–189. https://doi.org/10.1016/j.stem.2007.11.002.
88. Grimm, J.B., Muthusamy, A.K., Liang, Y., Brown, T.A., Lemon, W.C., Patel, R., Lu, R., Macklin, J.J., Keller, P.J., Ji, N., et al. (2017). A general method to fine-tune fluorophores for live-cell and in vivo imaging. Nat. Methods *14*, 987–994. https://doi.org/10.1038/nmeth.4403.
89. Mu, Y., Bennett, D.V., Rubinov, M., Narayan, S., Yang, C.-T., Tanimoto, M., Mensh, B.D., Looger, L.L., and Ahrens, M.B. (2019). Glia Accumulate Evidence that Actions Are Futile and Suppress Unsuccessful Behavior. Cell *178*, 27–43.e19. https://doi.org/10.1016/j.cell.2019.05.050.
90. Huang, F., Hartwich, T.M.P., Rivera-Molina, F.E., Lin, Y., Duim, W.C., Long, J.J., Uchil, P.D., Myers, J.R., Baird, M.A., Mothes, W., et al. (2013). Video-rate nanoscopy using sCMOS camera–specific single-molecule localization algorithms. Nat. Methods *10*, 653–658. https://doi.org/10.1038/nmeth.2488.
91. Liu, S., Mlodzianoski, M.J., Hu, Z., Ren, Y., McElmurry, K., Suter, D.M., and Huang, F. (2017). sCMOS noise-correction algorithm for microscopy images. Nat. Methods *14*, 760–761. https://doi.org/10.1038/nmeth.4379.
92. Mandracchia, B., Hua, X., Guo, C., Son, J., Urner, T., and Jia, S. (2020). Fast and accurate sCMOS noise correction for fluorescence microscopy. Nat. Commun. *11*, 94. https://doi.org/10.1038/s41467-019-13841-8.

93. Garyfallidis, E., Brett, M., Amirbekian, B., Rokem, A., van der Walt, S., Descoteaux, M., and Nimmo-Smith, I.; Dipy Contributors (2014). Dipy, a library for the analysis of diffusion MRI data. Front. Neuroinform. *8*, 8. https://doi.org/10.3389/fninf.2014.00008.

94. Kelly Buchanan, E., Kinsella, I., Zhou, D., Zhu, R., Zhou, P., Gerhard, F., Ferrante, J., Ma, Y., Kim, S., Shaik, M., et al. (2019). Penalized matrix decomposition for denoising, compression, and improved demixing of functional imaging data. Preprint at bioRxiv. https://doi.org/10.1101/334706.

95. Pedregosa, F., Varoquaux, G., Gramfort, A., Michel, V., Thirion, B., Grisel, O., Blondel, M., Prettenhofer, P., Weiss, R., Dubourg, V., et al. (2011). Scikit-learn: Machine Learning in Python. J. Mach. Learn. Res. *12*, 2825–2830.

96. Wei, Z., Inagaki, H., Li, N., Svoboda, K., and Druckmann, S. (2019). An orderly single-trial organization of population dynamics in premotor cortex predicts behavioral variability. Nat. Commun. *10*, 216. https://doi.org/10.1038/s41467-018-08141-6.

97. Gerstner, W., and Brette, R. (2009). Adaptive exponential integrate-and-fire model. Scholarpedia *4*, 8427. https://doi.org/10.4249/scholarpedia.8427.

98. Vladimirov, N., Wang, C., Höckendorf, B., Pujala, A., Tanimoto, M., Mu, Y., Yang, C.T., Wittenbach, J.D., Freeman, J., Preibisch, S., et al. (2018). Brain-wide circuit interrogation at the cellular level guided by online analysis of neuronal function. Nat. Methods *15*, 1117–1125. https://doi.org/10.1038/s41592-018-0221-x.

99. Virtanen, P., Gommers, R., Oliphant, T.E., Haberland, M., Reddy, T., Cournapeau, D., Burovski, E., Peterson, P., Weckesser, W., Bright, J., et al. (2020). SciPy 1.0: fundamental algorithms for scientific computing in Python. Nat. Methods *17*, 261–272. https://doi.org/10.1038/s41592-019-0686-2.

Please cite this article in press as: Kawashima et al., Voltage imaging reveals circuit computations in the raphe underlying serotonin-mediated motor vigor learning, Neuron (2025), https://doi.org/10.1016/j.neuron.2025.05.017

STAR★METHODS

KEY RESOURCES TABLE

REAGENT or RESOURCE	SOURCE	IDENTIFIER
Chemicals, peptides, and recombinant proteins		
alpha-bungarotoxin	Thermo Fischer Scientific	B1601
Dimethyl sulfoxide (DMSO)	Sigma	D8418
JF525 HaloTag Ligand	HHMI Janelia Research Campus	N/A
Anti-5HT rabbit polyclonal antibody	Sigma	Cat# S5545; RPID: AB_477522
Metronidazole	MP Biomedicals	02155710
Experimental models: Organisms/strains		
Zebrafish: *Tg(elavl3:iSeroSnFR)*	Haruvi et al.[24]	N/A
Zebrafish: *Tg(UAS:Voltron)*^{jf42Tg}	Abdelfattah et al.[26]	N/A
Zebrafish: *Tg(tph2:Gal4)*^{y228Tg}	Yokogawa et al.[48]	N/A
Zebrafish: *Tg(tph2:iGABASnFR)*	This study	N/A
Zebrafish: *Tg(tph2:SF-iGluSnFR)*	This study	N/A
Zebrafish: *Tg(gad1b:loxP-RFP-loxP-GFP)*^{nns26Tg}	Satou et al.[44]	N/A
Zebrafish: *Tg(elavl3:H2B-GCaMP6f)*^{jf7}	Dunn et al.[86]	N/A
Zebrafish: *Tg(elavl3:GCaMP6f)*^{jf1}	Dunn et al.[86]	N/A
Software and algorithms		
PyZebrascope	Barbara et al.[66]	Zenodo: https://doi.org/10.5281/zenodo.15301729
Cell segmentation	This study	Zenodo: https://doi.org/10.5281/zenodo.15293026
Custom Python scripts	This study	Zenodo: https://doi.org/10.5281/zenodo.15293043
FIJI (Image analysis)	NIH	https://imagej.net/software/fiji/
MapZebrain	Kunst et al.[40]	https://mapzebrain.org/home
Deposited data		
Processed data after cell segmentation	This study	Mendeley Data: https://doi.org/10.17632/3nn5t35j8s

EXPERIMENTAL MODEL AND STUDY PARTICIPANT DETAILS

Zebrafish husbandry

All zebrafish experiments were approved by the Institutional Animal Care and Use Committee (IACUC) at Janelia Research Campus, HHMI and the Institutional Animal Care and Use Committee (IACUC) and the Institutional Biosafety Committee (IBC) of the Weizmann Institute of Science and by the Israeli National Law for the Protection of Animals - Experiments with Animals (1994). Larvae were kept at a 10 h dark, 14 h light cycle at 28°C. Larval sex is not specified at this developmental stage and was therefore not determined.

Transgenic zebrafish

The transgenic zebrafish line that pan-neuronally expresses genetically-encoded serotonin indicator, *Tg(elavl3:iSeroSnFR)* (Figure 1), was generated in AB strain with Casper mutation[87] as described elsewhere.[24] To enhance the brightness, we use homozygous, in-crossed larvae at the age of 5-6 dpf. Transgenic zebrafish that express genetically-encoded voltage indicator, Voltron, (Figures 2 and 3) were obtained by crossing transgenic zebrafish that express Voltron under UAS promoter, *Tg(UAS:Voltron)*^{jf42Tg}[26], with transgenic zebrafish that express Gal4 transactivator under the tph2 promoter, *Tg(tph2:Gal4)*^{y228Tg}.[48] To label Voltron-expressing neurons with the accompanying fluorescent dye, 3-day-old embryos were incubated in dye solution [3.3 μM JF_{525}-HaloTag ligand[88] and 0.3% DMSO] in fish rearing water at room temperature for two hours. After screening for the fluorescence of the JF dye in the brain, the fish were returned to fish rearing water with food until the time of the experiment.

Please cite this article in press as: Kawashima et al., Voltage imaging reveals circuit computations in the raphe underlying serotonin-mediated motor vigor learning, Neuron (2025), https://doi.org/10.1016/j.neuron.2025.05.017

The dendritic morphology of serotonergic neurons (Figure 4A) was analyzed by creating dorsal and side projections from a transgenic zebrafish that sparsely expresses GFP, *Tg(tph2:Gal4; UAS:GFP)*. Transgenic zebrafish expressing a GABA indicator, iGABASnFR,[36] or a glutamate indicator, SF-iGluSnFR,[37] (Figure 4) were generated by cloning these genes in the direct downstream of the *tph2* promoter[48] on a Tol2 vector. These plasmids were injected into two-cell stage embryos of AB Casper mutant zebrafish with mRNA of Tol2 transposase to generate founder transgenic zebrafish. Experiments were performed using 5-6 dpf embryos generated by outcrossing F0 founder to AB Casper fish. GABAergic neurons in the DRN (Figures 5B and 6) were labeled using a transgenic zebrafish that expresses RFP in *gad1b*+ neurons, *Tg(gad1b:loxP-RFP-loxP-GFP)*$^{\mathrm{nns26Tg}}$. The anatomical co-labeling with serotonergic neurons (Figure 5B) used an anti-5-HT rabbit polyclonal antibody (Sigma, Cat # S5545; RPID: AB_477522) for immunostaining as described in our previous work.[17]

We analyzed the brain-wide neural response to visual feedback of swimming (Figures S5A–S5F) using transgenic zebrafish that express nuclear-localized calcium indicators under the pan-neuronal *elavl3* promoter,[17] Tg(*elavl3*:H2B-GCaMP6f)$^{\mathrm{jf7}}$. We performed high-speed calcium imaging in the raphe, thalamus and optic tectum (Figures S5G and S5H) using transgenic zebrafish that express cytosolic calcium indicators under the pan-neuronal elavl3 promoter,[17] *Tg(elavl3*:GCaMP6f)$^{\mathrm{jf1}}$.

METHOD DETAILS

Preparation for zebrafish imaging experiments

Imaging experiments were performed using 5- or 6-day larval zebrafish. The zebrafish was immobilized and mounted to an imaging chamber as described previously[17] with minor modifications. To detect small fluorescence changes of voltage and neurotransmitter indicators in the soma and dendrites of DRN serotonergic neurons (Figures 2, 3, 4, 6, S2, S4, and S8), we needed to stop the circulation to avoid shadowing effects of blood cells that pass through the excitation beam during the imaging.[26] For this purpose, the zebrafish were habituated in an artificial cerebrospinal fluid (ACSF) [in mM: 120 NaCl, 2.9 KCl, 2.1 $CaCl_2$, 1.2 $MgCl_2$, 20 $NaHCO_3$, 1.25 $NaHPO_4$, 10 Glucose] pre-bubbled with carbogen gas (95% O_2, 5% CO_2) for 30 minutes. The muscle of the zebrafish was then paralyzed by a short (up to 30 seconds) bath incubation with alpha-bungarotoxin (1 mg/ml, Thermo Fischer Scientific, B1601) dissolved in an external solution. After the fish became immobile, the heart movement of the zebrafish was stopped by microforceps to disrupt circulation. The zebrafish showed robust optomotor behavior in pre-bubbled ACSF for several hours. The zebrafish was further mounted to a custom-made chamber using 2% agarose (Sigma-Aldrich, A9414) and placed under a light-sheet microscope[65] with a 20x objective lens (Olympus, XLUMPLFLN). For serotonin imaging (Figure 1), we performed imaging experiments under a light-sheet microscope[66] with a 16x Objective lens (Nikon, CFI75 LWD) in normal fish-rearing water without using ACSF and heart surgery because of the lack of blood shadow artifacts in the dorsal hindbrain.

Light-sheet imaging

Imaging was performed in a light-sheet microscope according to a published design[65] with modifications targeted at optimizing Voltron imaging. To increase the fraction of time during which the imaged cells were illuminated by the excitation laser beam, the beam was expanded in the horizontal dimension using a pair of cylindrical lenses (LJ1878L1-A (f = 10 mm) and LJ1402L1-A (f = 40 mm), Thorlabs). Imaging was performed using a 488 nm excitation laser, a 562/40 emission filter for Voltron (Semrock, FF01-562/40) or a 525/50 emission filter for neurotransmitter indicators (Semrock, FF01-525/50), and a sCMOS camera (Hamamatsu, ORCA Flash4.0 v2). We used a frame rate of 300 frames/second for voltage imaging and 30 frames/second for neurotransmitter indicators. In this setup, the pixel dimension on the camera was 0.293 μm/pixel, and the imaged neurons occupied an area of 150-200 pixels on the image. For serotonin imaging (Figure 1), we used a 488 nm excitation laser, an emission filter for serotonin indicator (Semrock, FF03-525/50), and a frame rate of 30 frames/second. The pixel dimension of the camera (Hamamatsu, ORCA Fusion BT) was 0.406 μm/pixel.

Behavioral Assays in Virtual Reality

We simulated an environment in which the animals swim along a one-dimensional virtual track consisting of red and black bars (each 2 mm thick) perpendicular to the direction of swimming (Figure 1B) as previously described.[5,17,65] The visual effect of swimming was mimicked by accelerating the gratings backward when a fictive swim bout was detected. The visual environment slowly moved forward at the speed of 2 mm/s between swim bouts to visually simulate a backward movement of the fish due to the virtual backward water current. The fish swim against this virtual water current to stabilize their positions.[7] Thus, the forward velocity of the gratings is programmed as:

$$[\text{forward velocity}] = [\text{forward offset velocity}] - [\text{locomotor drive}] \times G_{ms}$$

(Figure 1B). During strong swim bouts, the visual environment moves backward, simulating a forward swimming of the fish. G_{ms} is a parameter controlling the amount of backward motion arising from fictive swimming and simulates action effectiveness.

We recorded swim signals (fictive swims) from the axonal bundles of spinal motoneurons in the tail by attaching a pair of large barrel electrodes to the left and right sides of the dorsal part of the tail. Signals were amplified by an amplifier (Molecular Devices, AxoClamp 700B or a combination of Intan RHD2132 chip and RHD2000 evaluation board) and recorded at 6 kHz using custom software written

Please cite this article in press as: Kawashima et al., Voltage imaging reveals circuit computations in the raphe underlying serotonin-mediated motor vigor learning, Neuron (2025), https://doi.org/10.1016/j.neuron.2025.05.017

in C# (Microsoft) or in Python. For synchronization between the swimming signals and neural activity imaging, camera trigger signals that initiate the acquisition of individual frames in the light-sheet microscope were recorded simultaneously with the swim signals. Individual swim events from electrode signals were detected according to a processing method described previously.[17] Briefly, the raw signals were high-pass filtered, squared and smoothed by applying a Gaussian filter (σ = 3.3 milliseconds). The resulting traces were defined to be the fictive swim signal (Figure 1B). Individual swim bouts were detected by finding the time points at which the swim signal crossed a threshold. This threshold was automatically set to lie just above a noise level based on a histogram of the swim signals.[5,65] Visual stimuli were delivered using a DLP projector (Picopix PPX-4010, Philips or LV130, Optoma) which has a low input lag of 16 milliseconds. The delay from fictive swim acquisition to the display of the gratings with the programmed velocity is about 35 ms in our virtual reality setup.

Behavioral tasks

Motor vigor learning

We examined the fish's behavior, neural responses, and neurotransmitter release during the motor vigor learning task (Figures 1, 2D, 3A–3E, 4C, 5, 6, S1A, S1A, S2B, S4C, S4D, and S8C–S8H), where fish receive visual feedback from swimming in closed loop and adapt their swim vigor to the motosensory gain G_{ms}. We alternated G_{ms} between low and high levels, each lasting 20 seconds. The value of high G_{ms} was chosen to be two to three times higher than that of low G_{ms},[5] and the value of low G_{ms} was set to the lowest value at which the zebrafish can stabilize their position in the virtual reality arena.

Visuomotor decoupling

We measured the neural activity of serotonergic neurons and glutamate release on their dendrites when the fish's swimming and visual flow resembling feedback are temporally decoupled (Figures 3F, 4G, 4H, S2D, and S2E). We designed three types of visuomotor events: closed-loop swimming (CL), swimming without any feedback (open-loop, OL) and replay of visual feedback without swimming (RE). In CL events, visual feedback was provided when the fish swam, using high G_{ms}. In the OL event, G_{ms} was set to zero, which resulted in no visual feedback in response to swimming. In the RE event, we replayed a backward visual motion pattern recorded in the preceding closed-loop epoch and only analyzed events that did not overlap with swimming. The latter two types of decoupling events were randomly presented among the closed-loop events. OL events occasionally triggered struggling-like swimming.[89] We excluded such events from the analysis and subsampled events with similar swim vigor as those in CL events. For RE events, we subsampled those that did not coincide with swimming.

We tested each fish in the motor adaptation task for 5 minutes before testing it in this task to ensure its capacity for responding to visual feedback and adapting their swim vigor.

Random gain/delay

We examined glutamate release on the dendrites of serotonergic neurons in the conditions where we [i] changed G_{ms} randomly at three levels (low, medium, high) for individual swim bouts (Figures 4E, 4F, S5G, and S5H) or [ii] delayed the visual feedback by three lags (0 ms, 200 ms, 400 ms) (Figures S4E and S4F). In the former task of varying G_{ms}, the medium G_{ms} was set to the average value of the low and high G_{ms}. In the latter task of varying delays, the delay was introduced randomly in 10% of the swim events for each of the delayed conditions. We tested each fish in the motor adaptation task for 5 minutes before testing it in these tasks to ensure its capacity for responding to visual feedback and adapting its swim vigor.

Short-term motor learning

This behavioral assay for testing the persistent learning effect (Figures S1D, S1F, and S2F) was previously described.[17] Briefly, the paradigm consisted of a 15-second initialization period with low G_{ms}, a 7-second or 30-second training period with high G_{ms}, a 10-second delay period with stopped visual stimuli, and a 5-second test period with medium G_{ms}. We performed 20 - 30 trials per recording session. The data in Figures S1D–S1F were acquired in the above study and re-analyzed for this study to compare with the prediction of the LAE model.

We also tested a variant of this behavioral assay to decouple swimming and visual feedback (Figure S3) to investigate whether training with visual feedback alone, without swimming for 30 seconds, has a similar learning effect to the above motor learning task. In half of the trials, visual feedback during the preceding 30-second training with high G_{ms} was replayed during the training period. To prevent the occurrence of swimming during the replay, only the backward component of the visual stimulus motion was replayed.

Processing pipeline for voltage imaging data

We built a data processing pipeline for voltage imaging data to automatically perform camera-noise correction, motion correction, denoising, and cell segmentation (Figure 2B).

Step #1: Camera-noise correction

We adopted the camera noise correction algorithm from refs. Huang et al.[90] and Liu et al.[91] The pixel readout is computed as

$$s_i = (s_i^r - o_i) / g_i$$

where s_i^r is the raw camera readout at pixel i, s_i is the corrected one, o_i is the camera offset, and g_i is the camera gain at pixel i. We estimated the offset o_i and baseline variance v_i in the no-light condition as the mean and variance of 60k images. The gain for each pixel was calculated as

$$g_i = \underset{g}{argmin} \sum_{k=1}^{K} \left(\left(v_i^k - v_i\right) - g\left(D_i^k - o_i\right)\right)^2,$$

where K is the total number of illumination levels acquired, k is the k^th illumination level, D_i^k and v_i^k are the mean and variance of the 20k images acquired in the k^th illumination level. In our setup, we measured them by varying the laser power from 0 mW (no light condition) to 18 mW. Empirically, we found that the camera-noise correction can improve motion correction and other later steps in the processing.[91,92]

Step #2: Motion correction

We performed the two-dimensional rigid registration of the images using a custom Python script based on the dipy package,[93] to correct drifts in the sequentially recorded images at the subpixel level.

Step #3: image-series denoising

We performed image-series denoising for motion-corrected video Y by finding its low-rank (at K) representation

$$\overline{Y_k} = \sum_{k=1}^{K} u_k v_k$$

with residual $R_k = Y - \overline{Y_k}$ is statistically white (within 99% confidence interval). Here, u_k, v_k are spatial and temporal components respectively and determined by the objective

$$u_k, v_k = \underset{u,v}{argmin} \| R_{k-1} - uv \|_F^{\,2}$$

where F denotes the Frobenius norm. This is equivalent to performing iterative principal components analysis (PCA) on Y and stopping the iteration at the k^th component as the residual is close to the white noise. Since the number of pixels is large, which creates difficulty in computing PCA, we alternatively divided the whole image into overlapped small patches (namely local PCA), performed this denoising procedure for each patch, and stitched the denoised patches back to a full denoised movie. Moreover, since video Y can be presented as a 3D tensor, we also tested the tensor-based optimization as

$$\overline{Y_k} = \sum_{k=1}^{K} u_{1,k} \circ u_{2,k} \circ v_k$$

where $u_{1,k}$ and $u_{2,k}$ are two spatial components along the vertical and horizontal directions of the imaging, respectively. We found that tensor decomposition would generate stripe-like spatial correlation horizontally (which might stem from the power fluctuation of the horizontal light-sheet illumination), and thus used local PCA instead throughout the denoising step.

Step #4: Cell segmentation

We performed cell segmentation on the denoised movie ($\overline{Y_k}$) using semi-nonnegative factorization, where

$$A, F, B = \underset{A,F,B}{argmin} \| \overline{Y_k} - AF - B \|_F^{\,2}$$

such that

$$A \geq 0, B = b \cdot 1^T, b \geq 0$$

where A is the matrix of the nonnegative components in which the pixels were connected in space (ROIs); F is the matrix of the temporal components and presents the fluorescent dynamics of ROIs, and B is the temporally constant background. We initialized the components using super-pixels,[94] which include the local pixels with neighboring correlations larger than 0.8. We then computed

$$\Delta F / F = \frac{F - F_0}{F_0}$$

for each component (or ROI), where baseline fluorescence F_0 is computed as a running 20% percentile of F within a 3-minute time window. In our hands, the denoising step does not affect the dynamics of spike generation (thus spike detection) or membrane potential fluctuation, compared to the computation of ΔF/F using hand-drawn ROIs. Since Voltron is a negative response indicator, we used the flipped signal (−ΔF/F) for subsequent analyses for spike detection and subthreshold activity estimation.

Step #5: Spike detection

We trained a machine-learning neural network (Figure 2C) in order to automatically extract the spikes from the time series data of ΔF/F. The network consists of two LSTM layers and a dropout layer that interconnects them. To train this neural network, we used simultaneous electrophysiology and imaging of cerebellar neurons expressing Voltron acquired in our previous work.[26] The goal of the network is to determine whether there is a spike event in the middle of the time series (the length of the time series is 41 frames or 136.67 ms) by minimizing the loss function of the cross-entropy between the prediction of spike from voltage imaging with the ground truth from the electrophysiology (Figure 2C; gray dots, ground truth from electrophysiology; black, prediction of the network).

Please cite this article in press as: Kawashima et al., Voltage imaging reveals circuit computations in the raphe underlying serotonin-mediated motor vigor learning, Neuron (2025), https://doi.org/10.1016/j.neuron.2025.05.017

We performed the 10-fold cross-validation in network training. We applied the trained network model to extract the spikes automatically thereafter.

Step #6: Subthreshold activity estimation

We estimated the subthreshold activity as a rolling median filter of time series data of ΔF/F with a window size of 70 ms. To avoid the nonlinearity of spikes (a depolarization followed by a repolarization), we clipped out the frames (from -1 to +1) around detected spikes while running the median filter.

Processing of neurotransmitter and neuromodulator imaging data

We adapted parts of the voltage imaging processing pipeline to automate the neurotransmitter and neuromodulator imaging processing, which included camera noise correction, motion correction, and denoising (Figure 2B).

Identification of regions of interest and estimation of dynamics in neurotransmitter and neuromodulator imaging data

After we obtained the denoised movie (which followed the same procedure as that in Voltron imaging processing, Figure 2B), we identified the super-pixels,[94] which include the local pixels with neighboring correlations larger than 0.8. We computed average fluorescence F inside all super-pixels (weighted equally) and then computed

$$\Delta F / F = \frac{F - F_0}{F_0}$$

for each movie, where the baseline fluorescence F_0 is computed as a running 20% percentile of F within a 3-minute time window.

Behavioral quantifications

Inclusion criteria

Zebrafish that do not show robust adaptation of swim vigor to the change of G_{ms} may have problems in perceiving the visual stimuli projected below the fish (Figure 1B) or may be developmentally defective. Therefore, we excluded fish whose swim vigor during high G_{ms} was not statistically lower than during low G_{ms} in the motor vigor learning, with a cut-off threshold of $p < 0.01$ using a one-sided rank-sum test.

Equalizing motor outputs at different G_{ms}

To disentangle the neural encoding of swim vigor and visual feedback, we subsampled the swim bouts with similar vigors at different G_{ms} to analyze "motor-equalized trials" (Figures 3D and 4E) as follows. We first computed the empirical cumulative distribution (ECD) of swim vigor across all swim bouts at a given G_{ms}. We then decided the overlapping range of swim vigor to subsample according to ECDs. Finally, we tweaked the subsample range for each G_{ms} to make sure that the average swim vigor of the subsamples was statistically identical across G_{ms} (Kruskal–Wallis test, $p > 0.05$). We applied this procedure to subsample trials in tasks of motor adaptation (Figure 3D), random G_{ms} (Figure 4E) and random visual-feedback delays (Figure S4E).

Adaptation levels of swim patterns

We quantified the ability to perform motor vigor learning before and after ablation of DRN GABAergic neurons or control GABAergic neurons (Figures 6H and S8H) as follows. We binned the swim vigor data at 300 Hz, and generated a vector of time series of swim vigor for 1 second, which is long enough to cover most swim patterns. We filled post-swim points in the vector as zeros. We then compared the moment-by-moment difference in swim vigor between low and high G_{ms} (Figure S8G). The cumulative period of time, where swim vigor was larger ($p < 0.05$, one-tailed rank-sum test) at low G_{ms}, was used to calculate the "adaptation level" of swimming between G_{ms}.

Kernel fits of membrane potential and spikes to behavioral variables

Response kernel estimation of serotonergic neurons based on behavioral variables (Figure 3E) was performed as follows. We predicted spike events and subthreshold membrane potentials from the behavioral variables of the time series of the swim vigor

$$S_t = \{s_t, s_{t-1}, s_{t-2}, \cdots, s_{t-\tau}\}$$

and that of the visual input

$$V_t = \{v_t, v_{t-1}, v_{t-2}, \cdots, v_{t-\tau}\}$$

and that of the recent spike events $SP_t = \{sp_t, sp_{t-1}, sp_{t-2}, \cdots, sp_{t-\tau}\}$, where sp is 0 or 1,at a given time t, allowing history dependence (t- τ) up to 300 time points (1 second). Since spiking activity is sampled at 300 Hz, for each single frame, the spike event is binary, we thus modeled the spike event as

$$P(spikes\ at\ time\ t) = Binomial\left(w_s{}^T S_t + w_v{}^T V_t - w_{sp}{}^T SP_t\right).$$

We optimized this probabilistic model from the data using a generalized linear model with logit link function and a l_2-form regularization on kernels of the swim vigor, i.e. w_s, the visual input, i.e. w_v, and the spike history, i.e. w_{sp}. The model was fitted in Python using l_2 logistic regression in the Scikit-learn package[95] with the following steps for data collection and cross-validation. The time series data was sampled randomly around spike events, with a balance of $P(spikes\ at\ time\ t) \simeq 0.5$. We determined the strength of l_2-form regularization using 5-fold cross-validation. In each fold, we held 20% of the data for validation (completely non-overlapped with the rest of the data in the original full time series) and used the remaining 80% of the data for training. Moreover, we used the square root form of the swim vigor data in fitting. We used a model without regularization on validation data as the full model and determined the performance, using negative log likelihood (NLL), as

$$1 - \frac{NLL(P_{est}(spikes))}{NLL(P_{true}(spikes))}.$$

This is equivalent to a measure of the explained variance in a logistic regression.

Furthermore, we assumed the change of subthreshold membrane potentials linearly as

$$\Delta F / F(t) - \Delta F / F(t-\tau) = k\left(w_s{}^T S_t + w_v{}^T V_t - w_{sp}{}^T SP_t\right) + c,$$

and thus the model error is

$$e(\Delta F / F(t)) = \Delta F / F(t) - \Delta F / F(t-\tau) - k\left(w_s{}^T S_t + w_v{}^T V_t - w_{sp}{}^T SP_t\right) + c,$$

where k and c are two scalars in model fits.

We then fit the combined model of spike events and the change of subthreshold membrane potential as

$$w_s, w_v, w_{sp} = \underset{w_s, w_v, w_{sp}}{arg\,min}\ NLL(P(spikes)) + \frac{1}{2}||e(\Delta F / F)||_2{}^2 + \frac{1}{2}\alpha\left(\|w_s\|_2{}^2 + \|w_v\|_2{}^2 + \|w_{sp}\|_2{}^2\right)$$

where α is l_2-form regularization of the kernels. We performed gradient descent-based minimization with the initialization of the parameters fitted from the spike-event-only model above.

Cell selections

Figure 3C included all segmented cells from gain adaptation tasks (Figure 1B) and memory tasks (Figure S1D; only using them in low and high G_{ms}) and ablation tasks (Figure 6; only using those before ablation) (we also fitted them all with the behavioral variables in Figure 3E). In Figure 3C, we sorted neurons based on their center of mass of spiking rates after swimming onset and separated them into high- or low-G_{ms} preferred categories.

Neural population codes

We computed the population coding of motor vigor learning by serotonergic neurons (Figures 6F and S8F) using a sparse version of linear discriminant analysis:[96]

$$l = \underset{l}{argmin} - \frac{\left(l^T\left(r_t{}^{high} - r_t{}^{low}\right)\right)^2}{l^T \Sigma_r l}.$$

Here r_t is n-dim vector of the neural activity at time t; n is the number of neurons in the population codes; $r_t{}^{high}$ and $r_t{}^{low}$ are the sample average of r_t at high or low G_{ms} conditions, respectively; l is the coding direction for high G_{ms}. We optimize the coding direction l with a l_2 regularizer, $\gamma \in [0,1]$, which was applied to the covariance matrix of the sample data

$$\Sigma_r = (1-\gamma)(r_t - <r_t>)(r_t - <r_t>)^T + \gamma I.$$

We sampled the data from the late phase of each G_{ms} period. The sample window for each data point to compute the firing rate is 1 second.

For the analysis of the neural population codes for G_{ms} in high-speed calcium imaging (Figure S5G), we used all identified neurons in each area (Figure S5H) and performed the following procedure. We first applied a Gaussian smoothing filter (σ = 3.3 ms) to all neural traces and then subtracted the baseline ΔF/F before the swimming (100 ms) from the ΔF/F values after the swimming in individual neurons for individual swim events. We then fitted a linear decoder by regressing the ΔF/F levels 500 ms after the swims, when the neural response sufficiently diverged, in all neurons to the ratio of G_{ms} values to that at low G_{ms} (1 = low, 2 = medium, 3 = high G_{ms}) in individual swim events. The resulting linear decoder was then applied to the population activity (ΔF/F values of all neurons) at individual time points around the onset of swims, and the first time point that showed a significant difference of this population vector between low and high G_{ms} conditions across swim events ($p < 0.01$) are designated as the response time.

Spiking neural network model

We simulated the neural network dynamics in the dorsal raphe nucleus (Figure 5) by using a spiking neural network model. Our model was equipped with 400 serotonergic neurons and 100 GABAergic neurons with sparse random connections with probability 0.03, i.e. $w^{jk} = 1$ if $p_c < 0.03$ and otherwise $w^{jk} = 0$ (where p_c is sampled from a uniform distribution from 0 to 1). The serotonergic neurons are modeled as adaptive integrate-and-fire neurons[97]:

$$C_m\, dV / dt = -g_L(V - E_L) - u + I$$

$$\tau_u du / dt = -a(V - E_L) - u$$

V is the membrane potential; u is the adaptation variable; I is the input current; $C_m = 0.5$ nF is the membrane capacitance; $g_L = 0.025$ uS is the leak conductance; $E_L = -60$ mV is the leak reversal potential; $a = 0.01$ uS is the adaptation coupling parameter (presenting the factor of the excitatory rebound currents) and $\tau_u = 200$ ms is the adaptation time constant for rebound currents). A spike happens when $V > V_{th} = -40$ mV, and V is then reset to -50 mV for a 2-ms refractory period; at the same time, a spike triggers an inhibitory afterhyperpolarization, which would add onto the adaptation variable,

$$u(t_{spike}) = u + b,$$

and b = 0.001 nA. GABAergic neurons are modeled as simple integrate-and-fire neurons:

$$C_m \, dV / dt = -g_L(V - E_L) + I$$

$$\text{with } C_m = 0.2 \text{ nF}; \; g_L = 0.02 \, \mu\text{S}; \; E_L = -60 \text{ mV}.$$

The synaptic inputs are modeled as

$$ds / dt = -\frac{1}{\tau_s} s + \sum_i \delta(t - t_i)$$

$$I_{syn} = g_{syn} s (V - V_{syn})$$

where g_{syn} is a synaptic conductance, V_{syn} is the synaptic reversal potential, and s is a synaptic gating variable (that increases by one at a presynaptic spike event, then decays at a time constant τ_s). We set $\tau_s = 50$ ms; $g_{5-HT} = 0.13$ ns; $V_{5-HT} = 0$ mV; $g_{GABA} = 0.52$ ns; $V_{GABA} = -70$ mV.

We provided glutamatic input into serotonergic and GABAergic neurons during the motor vigor learning task based on the results of neurotransmitter imaging. Both swim vigor and visual input were modeled as exponential decays from the behavioral variables' onset times:

$$I_B(t) = I_B{}^0 \exp\left(-\frac{t - t_B}{\tau_B}\right)$$

where the decay time constants were set to 50 ms, max input $I_B{}^0 = 100$ pA for swim vigor, $I_B{}^0 = 50$ pA for visual input. The total input to a kth serotonergic neuron was thus

$$I_k = \sum_{j \in 5-HT} w^{jk} I^{jk}_{5-HT} + \sum_{j \in GABA} w^{jk} I^{jk}_{GABA} + I_{vis}.$$

The total input to a kth GABAergic neuron was thus

$$I_k = \sum_{j \in 5-HT} w^{jk} I^{jk}_{5-HT} + \sum_{j \in GABA} w^{jk} I^{jk}_{GABA} + I_{swim}.$$

The currents I_{vis} and I_{swim} are assumed to arise from glutamatergic input targeting the serotonergic and GABAergic neurons, respectively, consistent with glutamate imaging under the assumption that the first glutamate wave arises from spillover from glutamatergic axons not targeting serotonergic neurons, which did not show a response to the first glutamate wave.

Two-photon, plasma ablation of DRN GABAergic neurons

We performed two-photon plasma ablation of DRN GABAergic neurons and voltage imaging of serotonergic neurons before and after the ablation (Figures 6 and S8) by using triple transgenic zebrafish, *Tg(tph2:Gal4; UAS:Voltron; gad1b:loxP-RFP-loxP-GFP),* and an optical setup described in our previous work.[98] Briefly, we first performed a volumetric scan of red fluorescence, which represents GABAergic neurons expressing RFP, using 561-nm CW laser (Omicron, Germany) and 630/92 nm filter (FF01-630/92, Semrock), to determine the site of ablation manually. Based on this acquired stack, we chose 40-70 GABAergic cells inside the DRN for the main ablation (Figure 6) or outside the DRN for control ablation (Figures S8C–S8F). The distribution of selected points is shown in Figures S8A and S8B. After the selection, we tuned the wavelength of a femtosecond laser (Camereon Ultra, Coherent) to 1050 nm and performed automatic ablation of selected cells. The lateral and depth positioning of the laser was controlled by a 2-axis galvanometer (Cambridge Technology) and a piezoelectric drive (Physik Instrument) of the objective lens. We chose the dwell time per cell to be 10-15 milliseconds because of the depth of this area. There are >100 GABAergic neurons in the larval zebrafish DRN,[17] and we did not target all of them to avoid the risk of collateral damage to nearby serotonergic neurons.

Please cite this article in press as: Kawashima et al., Voltage imaging reveals circuit computations in the raphe underlying serotonin-mediated motor vigor learning, Neuron (2025), https://doi.org/10.1016/j.neuron.2025.05.017

We performed voltage imaging of serotonergic neurons that express Voltron conjugated with JF525 fluorescent dye for 5 minutes during the motor vigor learning task before and after the above ablation procedure.

QUANTIFICATION AND STATISTICAL ANALYSIS

All statistical analyses were performed in Python using the Scipy package.[99] Statistical details of experiments, including the types of statistical tests and sample numbers, can be found in the figure legends. Briefly, we applied nonparametric statistics for comparisons: a signed-rank test for paired comparison and a rank-sum test for unpaired comparison, and a Kruskal–Wallis test for unpaired comparison across more than 2 conditions. For statistical analysis of firing rates of cells from multiple fish, we verified the sampling biases due to the fish identities using two-way ANOVA as

$$spike\ rate\ =\ C_{fish\ ID}+C_{condition}+C_{fish\ ID;condition}$$

where C is the constant depending on the fish ID, the conditions, and their interactions. For the condition is G_{ms} for Figure 3D and trial conditions for Figure 3F. We did not find any test above impacted by fish identity ("fish ID") ($p \geq 0.05$ for all). We used Spearman correlation to measure the correlation of neural variables with behaviors.

In addition to statistical analyses that we performed for individual data described in figure legends, we also quantified the statistical differences in the neural and behavioral effects between the ablation of raphe GABAergic neurons (here we call it “the target ablation”, Figure 6) and the ablation of control GABAergic neurons situated nearby but outside the raphe (here we call it “the control ablation”, Figure S8). The decreases in hyperpolarization after the target ablation (Figure 6D) were significantly larger than those after the control ablation (Figure S8C, $p = 2.3 \times 10^{-4}$, by rank sum test between neurons). The differences in spiking responses to different G_{ms} [Rate(high G_{ms})$-$Rate(low G_{ms})] in the post-swim time period (0.8 -1.0 s) after the target ablation (Figure 6E) were significantly smaller compared to those after the control ablation (Figure S8D, $p = 2.6 \times 10^{-5}$ by rank sum test between neurons). The differences in population coding to different G_{ms} in the target-ablated fish (Figure 6G) were also significantly smaller than those after the control ablation (Figure S8F, $p = 5.7 \times 10^{-3}$ by rank sum test between fish). The decreases in adaptation levels of swim vigor after the target ablation (Figure 6H) were significantly larger than those after the control ablation (Figure S8H, $p = 0.037$, rank sum test between fish).

Neuron, Volume *113*

Supplemental information

Voltage imaging reveals circuit computations in the raphe underlying serotonin-mediated motor vigor learning

Takashi Kawashima, Ziqiang Wei, Ravid Haruvi, Inbal Shainer, Sujatha Narayan, Herwig Baier, and Misha B. Ahrens

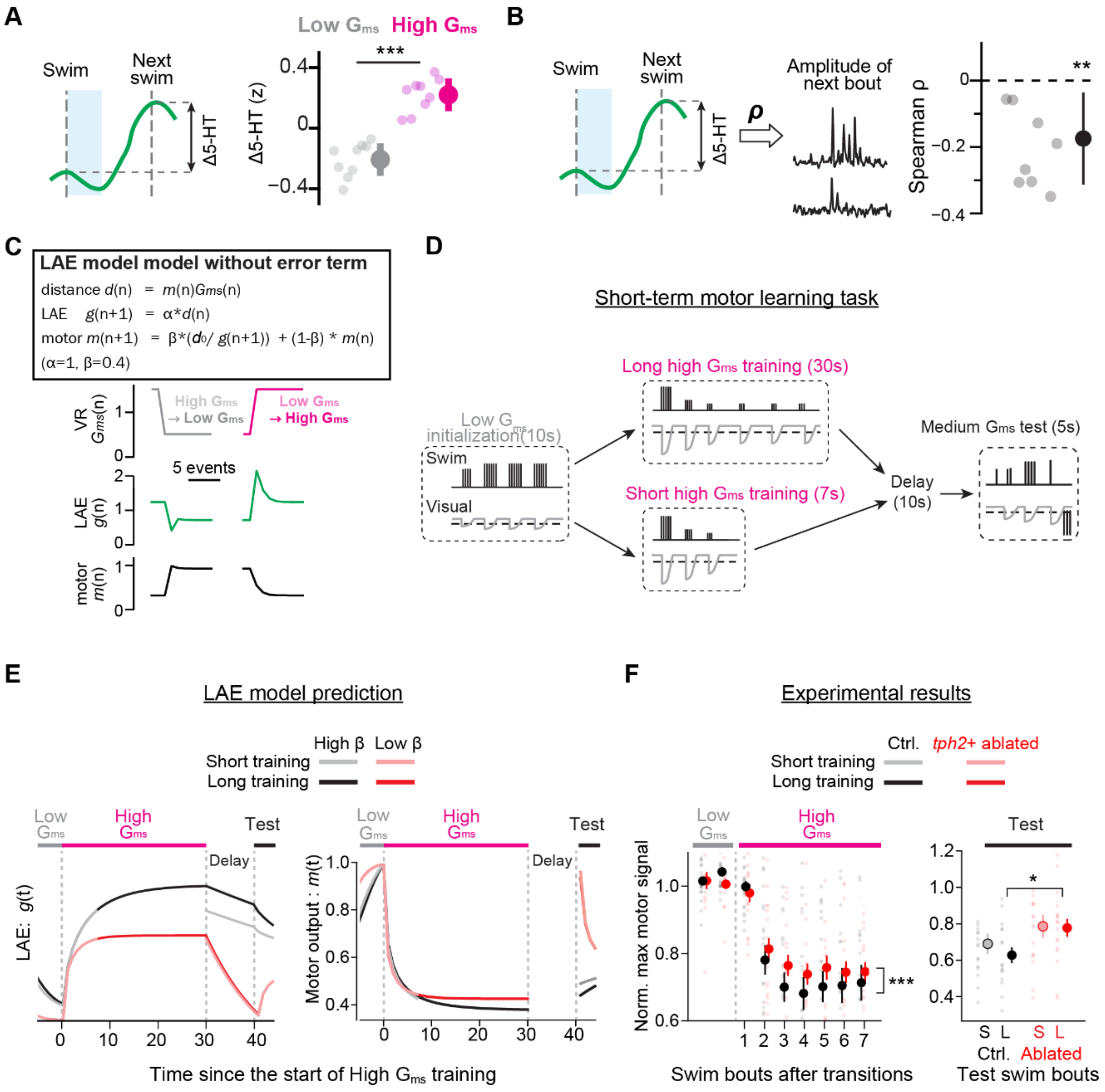

Figure S1: Serotonin release reflects the learned effectiveness of action and modulates motor vigor learning, related to Figure 1

(A) The post-swim increase of serotonin in the hindbrain ROI (Figure 1E), Δ5-HT, is high and positive in high G_{ms} (magenta) and low and negative in low G_{ms} (gray); error bars represent standard error of the mean (SEM) across N = 9 fish. ***p = 1.1 × 10^{-5}, two-tailed paired signed-rank test.

(B) The change in serotonin levels, Δ5-HT is negatively correlated with vigor of the next swim bout. Higher Δ5-HT corresponds to less vigorous subsequent swim bout; error bars represent SEM across N = 9 fish. **p = .0073, two-tailed signed-rank test against zero.

(C) Simulation of an alternative model for learning action effectiveness that does not involve error computation. *Left*, the formula of the alternative learned action effectiveness (LAE) model. *Right*, the result of the simulation for 10 swim episodes at the transition from low G_{ms} to high G_{ms}, and the transition from high G_{ms} to low G_{ms} during motor vigor learning. The temporal patterns of learned action effectiveness after changes in G_{ms} (middle) are significantly different from experimentally measured serotonin dynamics in the hindbrain of zebrafish (Figure 1D).

(D) Short-term motor learning paradigm for larval zebrafish. This behavioral paradigm from our previous work[17] tests not only the effects of changes in G_{ms} on swim vigor but also persistent behavioral effects of learned action effectiveness on swim vigor after a delay period. Swim vigor during the test period depends on the duration of the high G_{ms} training before the delay period.

(E) Simulation of the LAE model with error computation (Figure 1F) for the short-term motor learning paradigm in (D). Swimming occurs at 1 Hz. We simulated cases when the retention factor of the LAE model, β, was either high (0.98, black traces) or low (0.9, red traces). High β resulted in slow ramping of learned action effectiveness during the training and its slow decay during the delay period, which is qualitatively similar to the activity of raphe serotonergic neurons observed in our previous study. High β also resulted in [i] more suppression of swim vigor during the training and [ii] differences in swim vigor during the test period depending on the duration of the training. The duration of the delay period was simulated as 10 swim events, equivalent to about 10 seconds in real fish.

(F) Experimentally observed changes in swim vigor during the short-term motor learning paradigm in control fish (black) and fish whose *tph2+* raphe serotonergic neurons are ablated (red). The effects on swim vigor by the ablation are qualitatively similar to the simulation of the LAE model with a low β value in (E). Error bars represent SEM across $N = 17$ and 16 for control and ablated fish, respectively. ***$p = 6.4 \times 10^{-38}$ for the difference between the control and ablated groups by two-way ANOVA test with repeated measures. *$p = 0.034$ for the difference in test swim vigor after long training between the control and ablated groups by two-sample t-test. This is a re-analysis of published data from our previous work.[17]

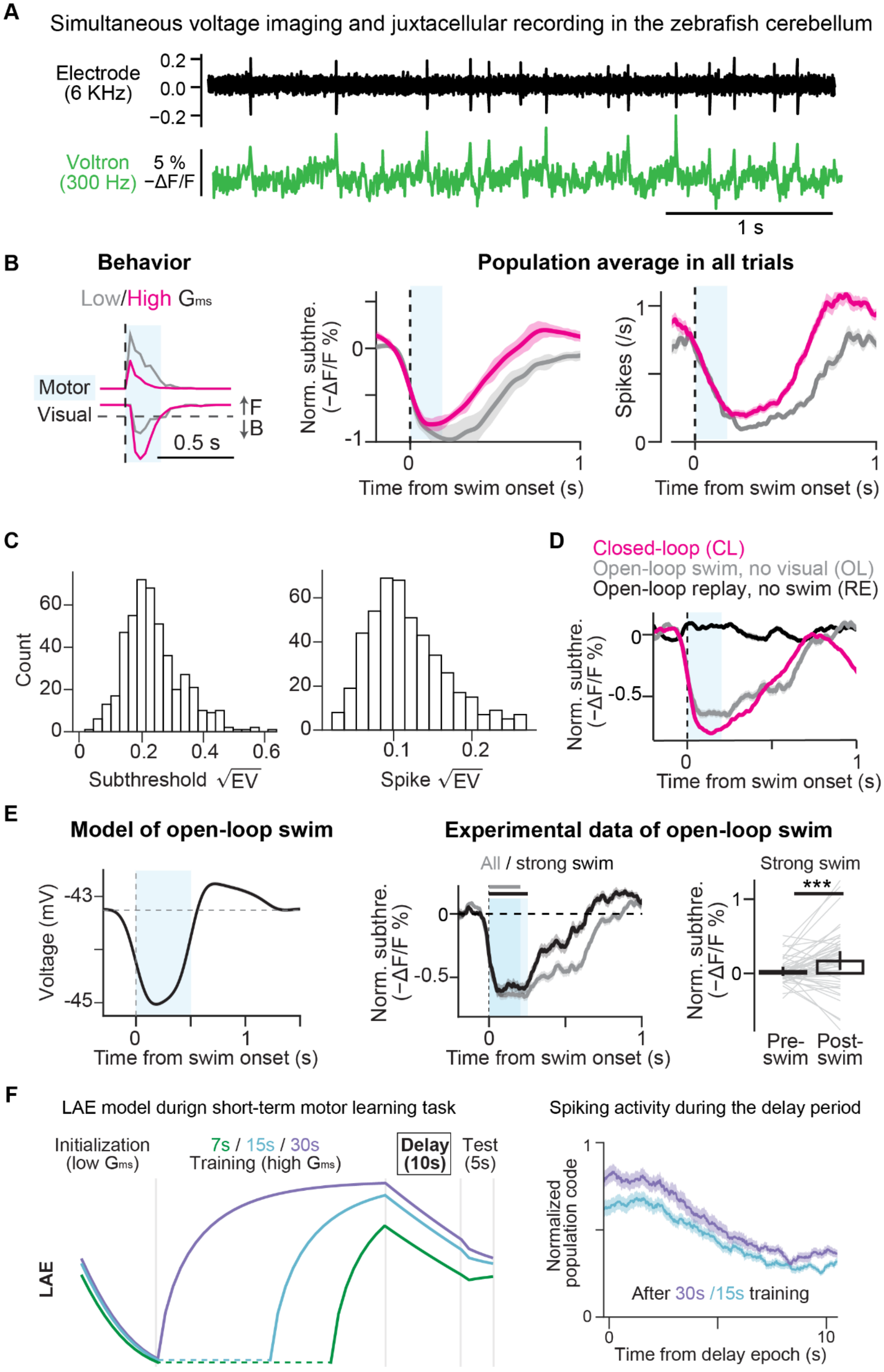
A
Simultaneous voltage imaging and juxtacellular recording in the zebrafish cerebellum
Electrode (6 KHz)
0.2
0.0
−0.2
Voltron (300 Hz)
5 % −ΔF/F
1 s
B
Behavior
Low/High Gms
Motor
Visual
↑F
↓B
0.5 s
Population average in all trials
Norm. subthre. (−ΔF/F %)
0
-1
Time from swim onset (s)
Spikes (/s)
1
0
Time from swim onset (s)
C
Count
60
40
20
0
0.2
0.4
0.6
Subthreshold √EV
0.1
0.2
Spike √EV
D
Closed-loop (CL)
Open-loop swim, no visual (OL)
Open-loop replay, no swim (RE)
Norm. subthre. (−ΔF/F %)
0
-0.5
1
Time from swim onset (s)
E
Model of open-loop swim
Voltage (mV)
-43
-45
Time from swim onset (s)
Experimental data of open-loop swim
All / strong swim
Norm. subthre. (−ΔF/F %)
0
-0.5
Time from swim onset (s)
Strong swim
***
1
0
Pre- swim
Post- swim
F
LAE model durign short-term motor learning task
Initialization (low Gms)
7s / 15s / 30s Training (high Gms)
Delay (10s)
Test (5s)
LAE
Spiking activity during the delay period
Normalized population code
1
0
After 30s /15s training
10
Time from delay epoch (s)

Figure S2: Supporting materials of spiking and voltage dynamics, related to Figures 2 and 3

(A) Signal traces of simultaneous voltage imaging and electrophysiology in eurydendroid cells in the zebrafish cerebellum, which were used for developing neural networks for spike detection in Figure 2C. This data was acquired in our previous work.[26]

(B) Swim-triggered average of behavioral traces, membrane potential and spiking dynamics in serotonergic neurons during motor vigor learning. Compared to the motor-equalized analysis presented in Figure 3D, here we present the triggered averages of all swim events. Shading represents SEM across swim events.

(C) Distribution of explained variance for subthreshold membrane potential and spiking activity for the model fitting shown in Figure 3E.

(D) Swim-triggered (magenta, gray) or visual-triggered (black) averages of membrane potential dynamics for closed-loop or open-loop experiments presented in Figure 3F. We subsampled swim events to equalize swim vigor between closed-loop and swim-only events for this analysis. Shading represents SEM across swim events.

(E) Rebound excitation during open-loop events in the serotonergic neurons. Simulation (left, see Figure 5 for details) and experimental data (right) are presented. We subsampled open-loop swim events with strong vigor from the dataset of Figure 3F and S2D to investigate the effects of rebound excitation after motor-evoked inhibition (black line). The same plot of Figure S2D from all swim events is also shown for comparison (gray line). Shading and error bars represent SEM across 51 high-G_{ms} cells from *N* = 7 fish. ***$p < .0001$, paired signed-rank test in comparison of pre- versus post-swim membrane potential during strong swimming events.

(F) *Left*, model predictions of LAE dynamics during the short-term motor learning paradigm with different training conditions. Purple, 30 seconds of high G_{ms} training; blue, 15 seconds; green, 7 seconds; navy, no training or replay. $\alpha = 0.10$, $\beta = 0.02$ in this simulation. *Right*, voltage imaging data. Population dynamics of raphe serotonergic neurons during the delay period are qualitatively consistent with the LAE model predictions. The population vector is calculated in the same way as Figure 6G for *N* = 8 fish (see Methods). For each fish, 8 to 41 neurons (25±8, mean ± sd) were used to calculate this vector. Shading represents SEM across fish.

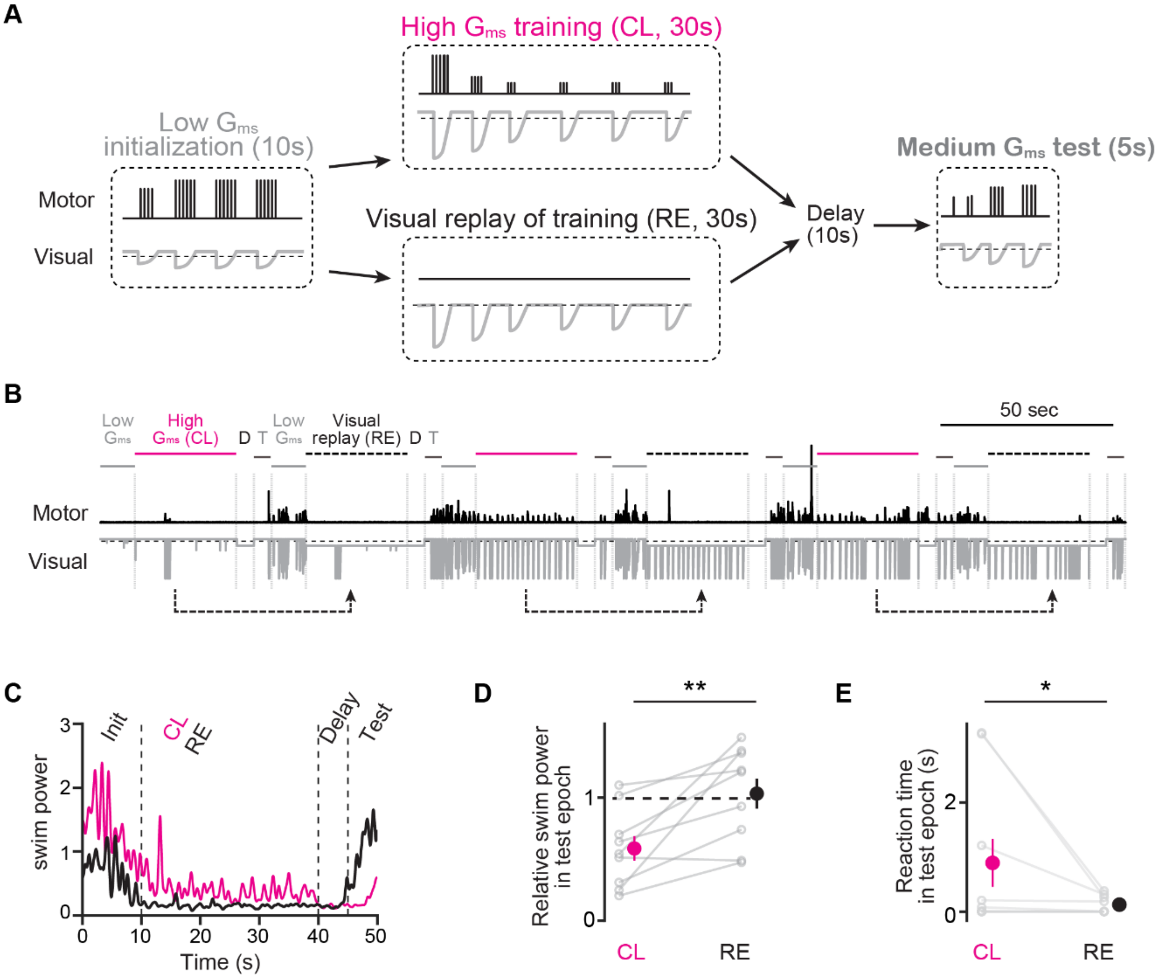

Figure S3. Less learning effects from swim-decoupled visual feedback during the short-term motor learning paradigm, related to Figure 3F

(A) Motor learning task that compares the learning effects of swim-coupled, closed-loop visual feedback (CL, top) and swim-decoupled, replayed visual feedback (RE, bottom). To prevent the occurrences in coincident swimming, we only replayed the backward component of the visual motion during the replay period.

(B) Task structure (top), swimming patterns (middle) and visual stimuli motions (bottom) in 3 consecutive trials of the behavioral paradigm presented in (A). Of note, the fish swim very little during the replay in our analysis.

(C) Average swim pattern during high G_{ms} closed-loop training period (magenta) and replay period (black) of an example fish.

(D) Swim vigor decreases after high G_{ms} training but remains unchanged after the replay. *N* = 9 fish. ***p* = .0078, paired signed-rank test. Error bars represent SEM across fish.

(E) Reaction time becomes longer after G_{ms}. *N* = 9 fish. **p* = .028, two-tailed paired signed-rank test. Error bars represent SEM across fish.

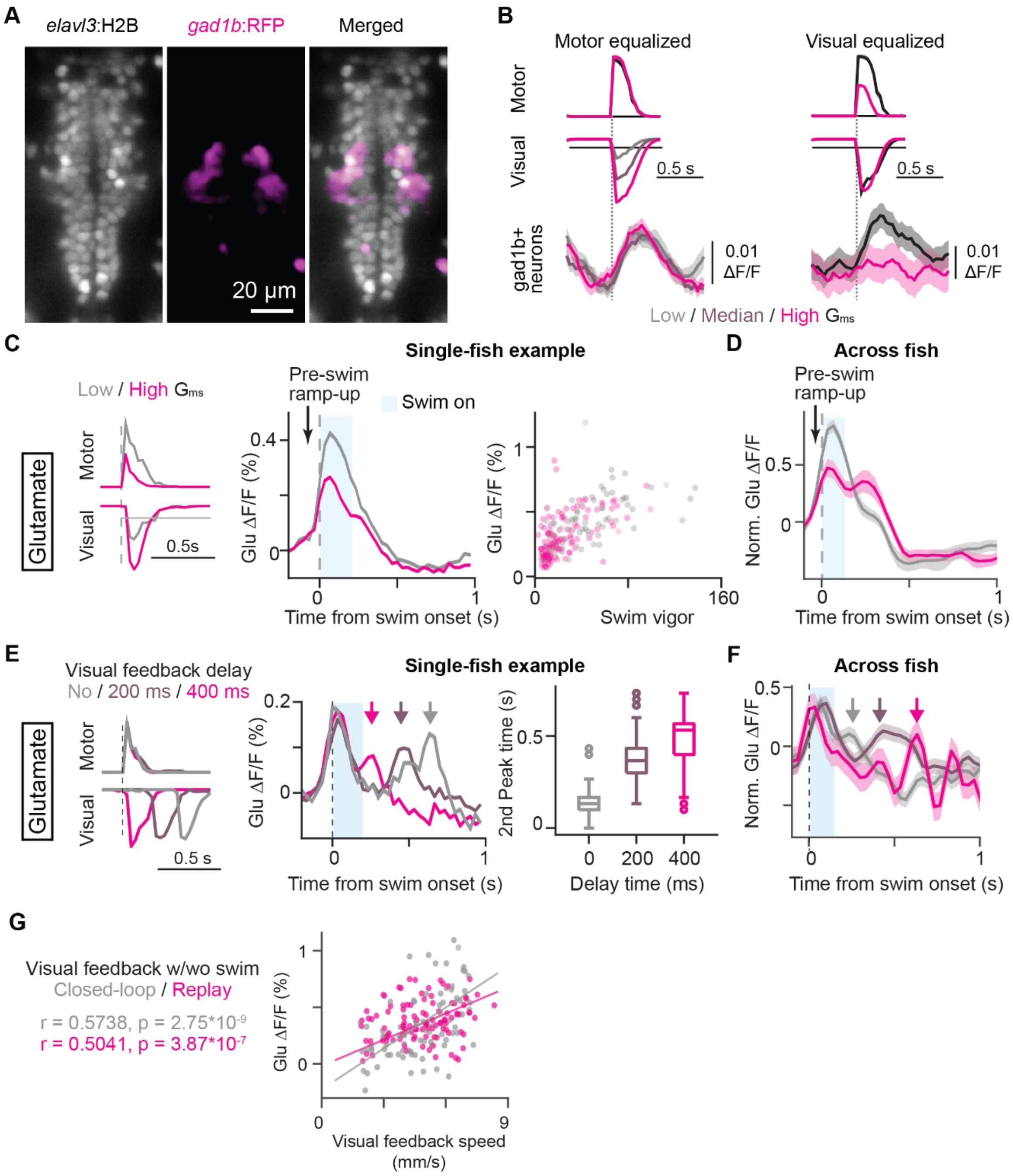

Figure S4: Supporting data for neurotransmitter imaging in the dendrites of serotonergic neurons, related to Figure 4

(A) Anatomy of raphe GABAergic neurons in the raphe nucleus that express red fluorescent protein (RFP) downstream of the *gad1b* promoter in a transgenic zebrafish. **(B)** Raphe GABAergic neurons typically encode swim vigor rather than the velocity of visual feedback. Shadings represent SEM across $N = 8$ fish. (A, B) are replots of data collected in our previous study.[17]
(C,D) Swim-triggered averages of glutamate inputs into the dendrites of raphe serotonergic neurons in an example fish (C) and across fish (D) during the motor vigor learning paradigm. Unlike the analysis presented in Figure 4E, we did not subsample swimming events to equalize swim vigor across different G_{ms} conditions in this analysis. $N = 17$ fish for cross-fish analysis in (D). Shadings represent SEM across fish.

(E) Temporal shifts of glutamate inputs during delayed visual feedback of swimming. Example from a single fish. We equalized the vigor of swim bouts across conditions of a variable delay of visual feedback randomly given at 0ms, 200 ms, or 400 ms. *Right*, the second peak of the glutamate inputs shifted according to the set delays accordingly.

(F) Cross-fish average of glutamate inputs in response to temporal delays of visual feedback after swimming shown in (E). *N* = 2 fish, 6 sessions. Shading represents SEM across sessions.

(G) Visually evoked glutamate inputs that occur in the absence of motor actions (Figures 4G,H) are correlated with visual speed. Example from a single fish. Gray, closed-loop; magenta, open-loop replay trial with no swimming.

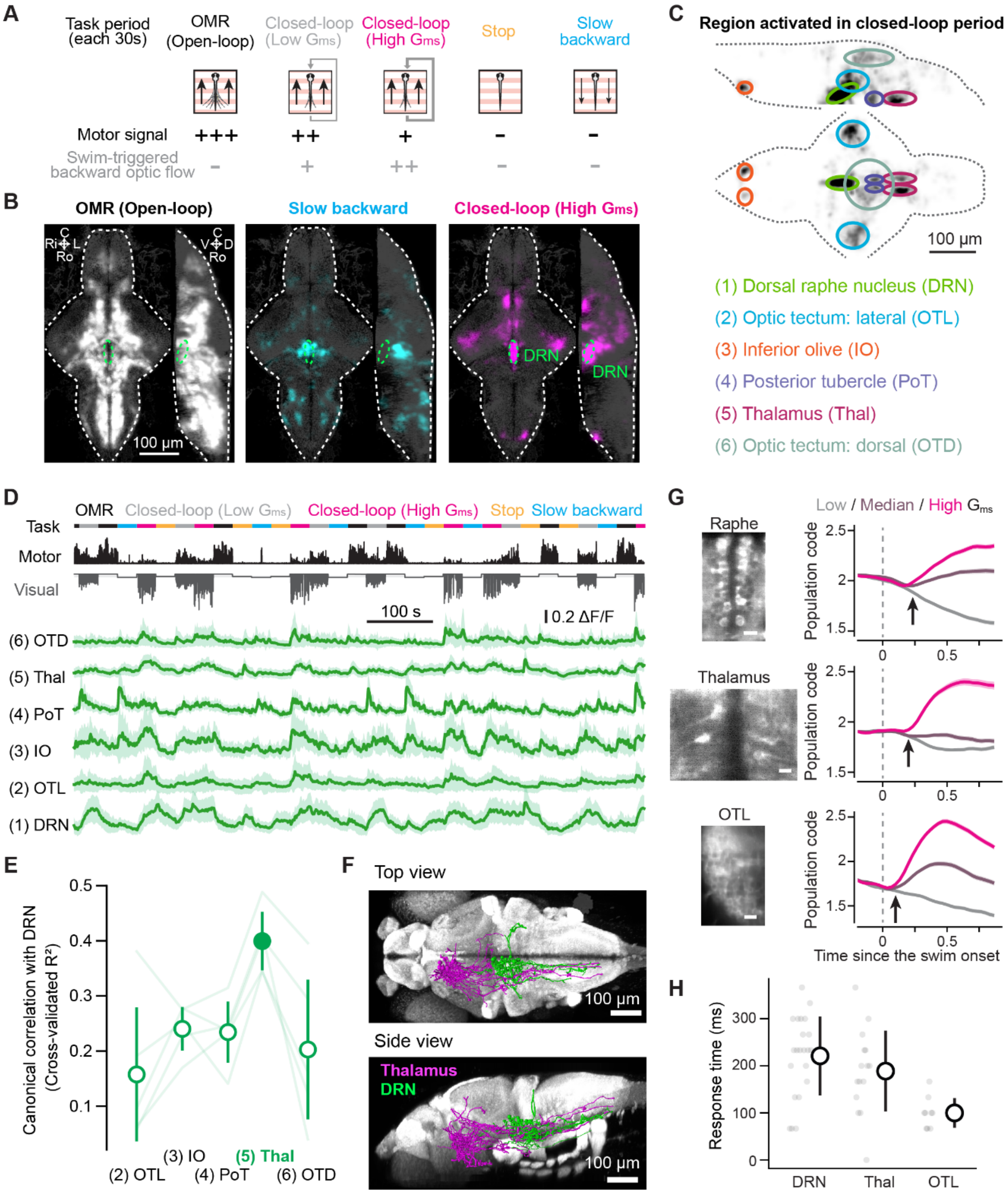

Figure S5: Potential upstream brain area that sends visual information to raphe, related to Figure 4

(A) The behavioral task for identifying neurons activated by closed-loop sensory feedback. In the OMR (open-loop) period, the visual environment moves forward without any feedback. In the 'Closed-loop' period, the visual environment moves forward, but when a swim signal is detected it moves backward with low (gray) or high (magenta) G_{ms}. In the 'Stop' or "Slow backward" period, the visual environment stops or slowly moves backward, during which the fish tend to swim less or cease swimming.

(B) Whole-brain maps of neurons that showed highest activity in the OMR (open-loop) period (white), in the Slow backward period (cyan), or in the closed-loop high G_{ms} period (magenta) morphed and overlaid on a reference brain (gray). *N* = 5 fish. See Methods and Resources for details of analyses. D, dorsal; V, ventral; Ro, rostral; C, caudal; Ri, right; L, left.

(C) Anatomical segmentation of brain regions that showed the highest activity in the closed-loop G_{ms} period. *Top*, the same whole-brain map in **(**B**)** inverted for brightness and overlaid with anatomical masks. *Bottom*, a list of six identified regions. Brain areas showing G_{ms} encoding include: dorsal raphe nucleus (DRN), lateral optic tectum (OTL), dorsal optic tectum (OTD), posterior tubercle (PoT), thalamus (Thal) and inferior olive (IO). (A)-(C) are re-adapted from the supplementary figure of our previous work.[17]

(D) Population activity dynamics of six brain areas identified in (C). We extracted neurons that show the highest activity during the closed-loop (high G_{ms}) period from each area and plotted their average activities from a representative fish. Shading represents standard deviation across extracted neurons for individual areas.

(E) Canonical correlation analysis between population dynamics of brain areas identified the thalamus as a potential upstream area of the DRN. For each fish, we extracted neurons that show the highest activity during the closed-loop (high G_{ms}) period from each area and calculated cross-validated canonical correlation (R^2) to neural populations in the DRN. We then further averaged these values across 5 fish. Error bars represent SEM across fish.

(F) Single-cell projections from the thalamus (magenta) spatially overlap with the dendrites of raphe serotonergic neurons (green). We used the single-cell projection atlas from Kunst *et al*., 2019.[42]

(G) High-speed calcium imaging revealed delayed visual response in the thalamus and raphe compared to the optic tectum. In this experiment, fish swam with randomly changing G_{ms} as in Figure 4E while we performed calcium imaging using cytosolic GCaMP6f indicators in individual areas. Different areas were imaged in different sets of fish. We quantified response times as the timing after swim onset when a significant difference in neural responses to different G_{ms} conditions appears by calculating population codes for G_{ms} (see Methods). *Left*, representative imaging plane in individual areas. Scale bar, 10 µm. *Right*, dynamics of population codes for G_{ms} aligned to the onsets of swims in a representative fish for each area. Shading represents SEM across swim events. Black arrows indicate the onset of statistically significant response differences between low and high G_{ms} conditions for individual fish.

(H) Summary of estimated response time in the raphe, thalamus, and optic tectum. Raphe (DRN), 220 ± 83 ms (mean ± standard deviation across fish; each dot represents each fish) from $N = 22$ fish. Thalamus (Thal), 188 ± 85 ms from $N = 15$ fish. Optic tectum (OTL, optic tectum lateral), 99 ± 31 ms from $N = 9$ fish. The data of the raphe nucleus is a re-analysis of data presented in our previous work[17]. The data for other areas were acquired in the same period as the raphe nucleus.

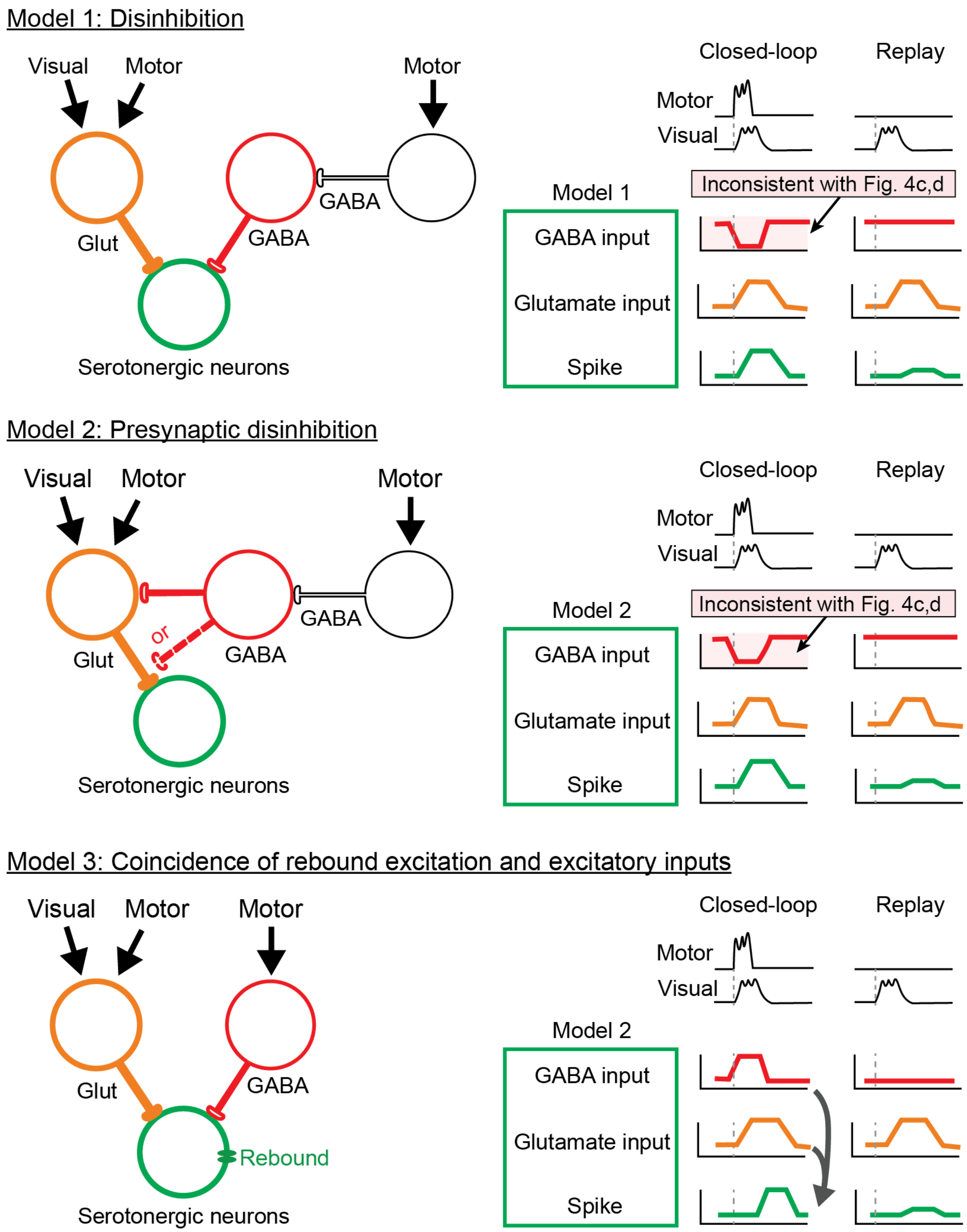

Figure S6: Candidate circuit models for sensory-motor computations in serotonergic neurons, related to Figure 5

Hypothetical circuit models of motor-gated sensory responses in raphe serotonergic neurons. *Left*, we formulated models based on somatic disinhibition (Model 1), presynaptic disinhibition (Model 2), and coincidence of rebound excitation and synaptic inputs (Model 3). *Right,* schematics of expected input patterns of GABA and glutamate. Only Model 3 is consistent with our experimental observation of GABA and glutamate inputs in Figure 4. These model schematics do not represent an exhaustive list of possibilities.

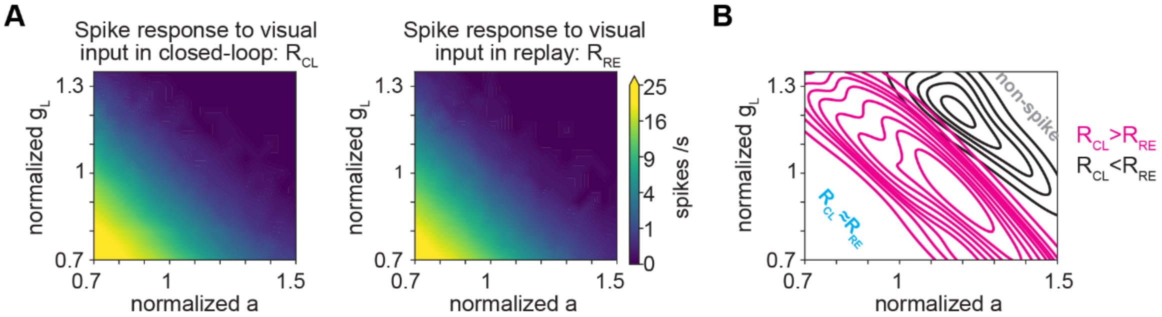

Figure S7. Parameter sensitivity of spiking neuronal network model and comparison of model prediction with real data, related to Figure 5

(A,B) Model dynamics in parameters *a*-g_L space, where *a* represents the rebound current and g_L represents leak conductance. (A) Model spike response to visual input in closed-loop (R_{CL}, left; with inhibitory input before visual inputs) and replay (R_{RE}, right; without inhibitory input before visual inputs) conditions. (B) The difference between R_{CL} and R_{RE}. Magenta, coincidence detection regime, where R_{CL} is higher than R_{RE}; black, simple-sum-of-two-inputs model regime, where R_{CL} is lower than R_{RE}. Coincidence detection works at low spike rate regimes, while R_{CL} and R_{RE} are of small difference at high spike rate regimes.

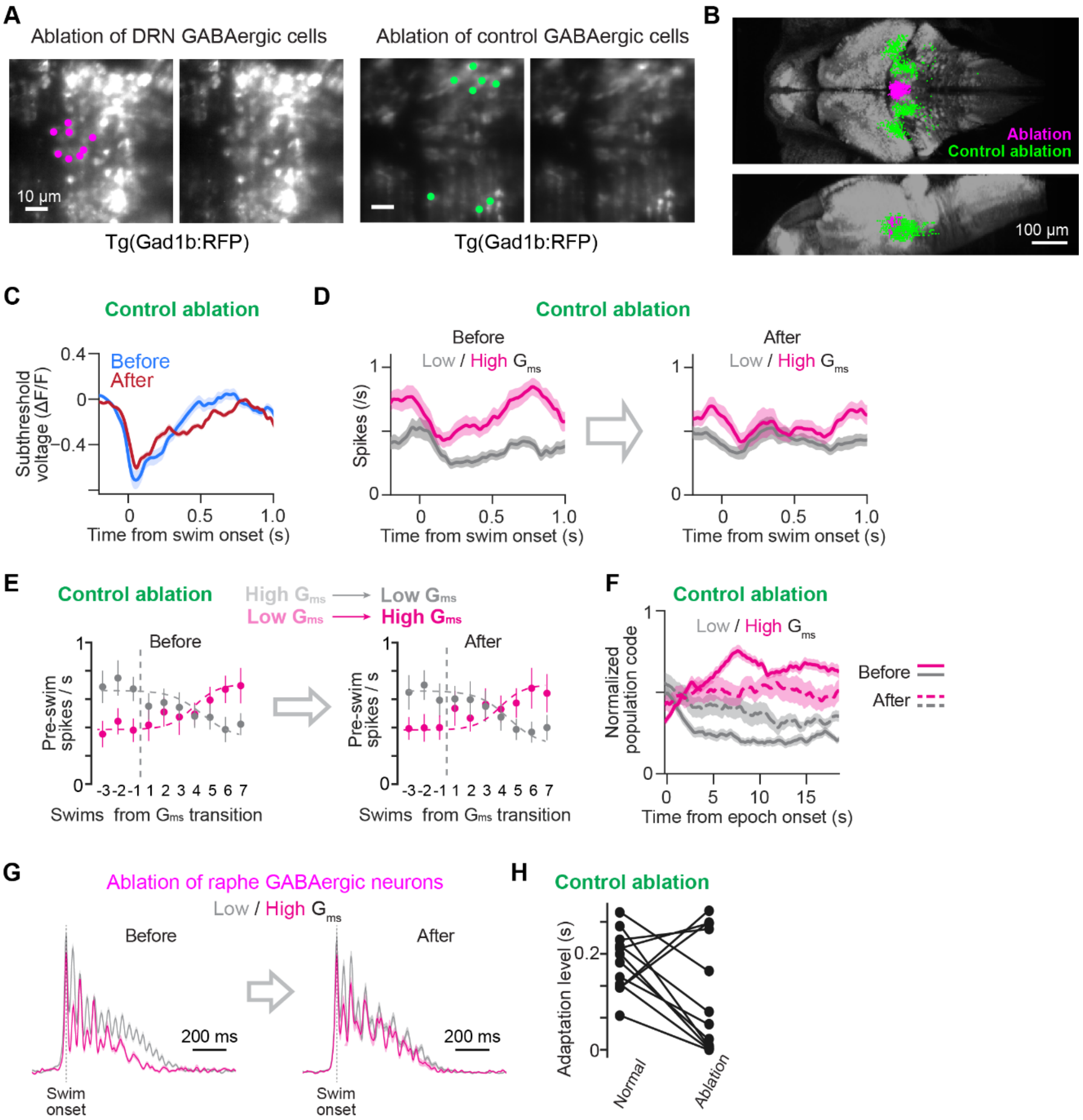

Figure S8. Supplementary materials for ablation of GABAergic neurons in DRN, related to Figure 6

(A,B) Anatomical loci of the ablation of raphe GABAergic neurons (magenta), presented in Figure 6, and the control ablation of GABAergic neurons outside the raphe nucleus (green), presented in (C)-(F). (A) Representative loci of two-photon plasma ablation in individual fish. (B) Summary of ablation loci for N = 8 and 10 fish for the ablation of raphe GABAergic neurons (magenta) and GABAergic neurons outside the raphe (green), respectively.

(C) Changes of membrane potential dynamics in serotonergic neurons before and after the control ablation. We did not see major reduction of swim-evoked inhibition after the control ablation compared to what we observed after the ablation of raphe GABAergic neurons in Figure 6D. N = 10 fish, 57 high G_{ms} cells. Shading represents SEM across cells.

(D) The control ablation of GABAergic neurons outside the raphe nucleus resulted in only partial loss of visual feedback encoding after swimming. *Left*, spiking in serotonergic neurons before the control ablation during low (gray) and high (magenta) G_{ms}. *Right*, spiking in 5-HT neurons in the same animals after the control ablation. N = 10 fish, 57 high G_{ms} cells. Shading represents SEM across cells.

(E) The control ablation of GABAergic neurons outside the raphe nucleus did not abolish the slow accumulation of tonic baseline firing in serotonin neurons, as compared to the ablation of raphe GABAergic neurons in Figure 6F. Magenta, from low G_{ms} to high G_{ms}; gray, from high G_{ms} to low G_{ms}. Left, before ablation; right, after ablation. Duration of 10 swim bouts from -3rd swim event to +7th swim event before ablation is about 18.26±7.99 s (mean±sd); that after ablation is about 25.06±12.07. Dash lines, sigmoid. *N* = 10 fish, 57 high G_{ms}-preferred cells. The pre-swim spike rates can encode LAE g_t over >10 sec even after control ablation. Error bars represent SEM across cells.

(F) DRN serotonergic neurons retain population coding of *L*AE after the control ablation over swim events, compared to the ablation of raphe GABAergic neurons in Figure 6G. *N* = 10 fish, 20 sessions. Shading represents SEM across sessions.

(G) The average trace of swim signals during low G_{ms} (gray) and high G_{ms} (magenta) from a representative fish before and after the ablation of raphe GABAergic neurons. The number of time points that show significant differences between low and high G_{ms} was used to quantify the “adaptation levels” in Figure 6H and S8H. *N* = 148 and 94 bouts for low and high G_{ms} conditions before the ablation, and *N* = 115 and 55 bouts for low and high G_{ms} conditions after the ablation. Shading represents SEM across swim bouts.

(H) The control ablation of GABAergic neurons outside the raphe nucleus did not cause a reduction in motor adaptation. *N* = 12 fish, *p* = .129, paired signed-rank test in comparison of before and after the ablation. The average adaptation level across fish is 0.1376 ± 0.064 before ablation and 0.1077 ± 0.086 after ablation (the swim duration increased from 0.1588 ± 0.014 s to 0.2302±0.038 s before vs after ablation).